

 Open access • Journal Article • DOI:10.1007/S11356-019-04128-Y

## Elucidating the dechlorination mechanism of hexachloroethane by Pd-doped zerovalent iron microparticles in dissolved lactic acid polymers using chromatography and indirect monitoring of iron corrosion — [Source link](#)

[Romain Rodrigues](#), [Stéphanie Betelu](#), [Stéfan Colombano](#), [Guillaume Masselot](#) ...+2 more authors

**Published on:** 16 Jan 2019 - [Environmental Science and Pollution Research](#) (Springer Berlin Heidelberg)

**Topics:** [Zerovalent iron](#) and [Desorption](#)

Related papers:

- [Dechlorination of tetrachloroethylene in water using stabilized nanoscale iron and palladized iron particles](#)
- [Continuous rapid dechlorination of p-chlorophenol by Fe-Pd nanoparticles promoted by procyanidin](#)
- [Hydrodechlorination of 2,4,6-trichlorophenol for a permeable reactive barrier using zero-valent iron and catalyzed iron](#)
- [Doping of biogenic Pd catalysts with Au enables dechlorination of diclofenac at environmental conditions](#)
- [\[Reductive dechlorination of 4-chlorophenol using nanoscale iron\]](#).

Share this paper:    

View more about this paper here: <https://typeset.io/papers/elucidating-the-dechlorination-mechanism-of-hexachloroethane-3q2v4w5nbx>



**HAL**  
open science

# Elucidating the dechlorination mechanism of hexachloroethane by Pd-doped zerovalent iron microparticles in dissolved lactic acid polymers using chromatography and indirect monitoring of iron corrosion

Romain Rodrigues, Stéphanie Betelu, Stefan Colombano, Guillaume Masselot, Théodore Tzedakis, Ioannis Ignatiadis

## ► To cite this version:

Romain Rodrigues, Stéphanie Betelu, Stefan Colombano, Guillaume Masselot, Théodore Tzedakis, et al.. Elucidating the dechlorination mechanism of hexachloroethane by Pd-doped zerovalent iron microparticles in dissolved lactic acid polymers using chromatography and indirect monitoring of iron corrosion. *Environmental Science and Pollution Research*, Springer Verlag, 2019, 26, pp.7177-7194. 10.1007/s11356-019-04128-y . hal-02380709

**HAL Id: hal-02380709**

**<https://hal.archives-ouvertes.fr/hal-02380709>**

Submitted on 15 May 2020

**HAL** is a multi-disciplinary open access archive for the deposit and dissemination of scientific research documents, whether they are published or not. The documents may come from teaching and research institutions in France or abroad, or from public or private research centers.

L'archive ouverte pluridisciplinaire **HAL**, est destinée au dépôt et à la diffusion de documents scientifiques de niveau recherche, publiés ou non, émanant des établissements d'enseignement et de recherche français ou étrangers, des laboratoires publics ou privés.

1 Elucidating the dechlorination mechanism of hexachloroethane by Pd-doped  
2 zero-valent iron microparticles in dissolved lactic acid polymers using  
3 chromatography and indirect monitoring of iron corrosion

4 Romain Rodrigues<sup>1,2,3\*</sup>, Stéphanie Betelu<sup>1</sup>, Stéfan Colombano<sup>1</sup>, Guillaume Masselot<sup>2</sup>, Theodore Tzedakis<sup>3</sup>,  
5 Ioannis Ignatiadis<sup>1</sup>

6 1: BRGM (French Geological Survey), 3 avenue Claude Guillemin, 45060 Orléans Cedex 2, France.

7 2: ADEME (French Environment and Energy Management Agency), 20 avenue du Grésillé, 49000 Angers  
8 Cedex 1, France.

9 3: LGC (Chemical Engineering Laboratory), 118 route de Narbonne, 31062 Toulouse Cedex 9, France.

10 \* Corresponding author: [romain.rodriques64@gmail.com](mailto:romain.rodriques64@gmail.com)

## 11 Abstract

12 The degradation mechanism of the pollutant hexachloroethane (HCA) by a suspension of Pd-doped zero-valent  
13 iron microparticles (Pd-mZVI) in dissolved lactic acid polymers and oligomers (referred to as PLA), was  
14 investigated using gas chromatography and the indirect monitoring of iron corrosion by continuous  
15 measurements of pH, oxidation-reduction potential (ORP) and conductivity. The first experiments took place in  
16 the absence of HCA, to understand the evolution of the Pd-mZVI/PLA/H<sub>2</sub>O system. This showed that the  
17 evolution of pH, ORP and conductivity is related to changes in solution chemistry due to iron corrosion, and that  
18 the system is initially cathodically controlled by H<sup>+</sup> mass transport to Pd surfaces because of the presence of an  
19 extensive PLA layer. We then investigated the effects of Pd-mZVI particles, temperature, initial HCA  
20 concentration and PLA content on the Pd-mZVI/PLA/HCA/H<sub>2</sub>O system, to obtain a better understanding of the  
21 degradation mechanism. In all cases, HCA dechlorination first requires the production of atomic hydrogen H<sup>\*</sup>—  
22 involving the accumulation of tetrachloroethylene (PCE) as an intermediate—before its subsequent reduction to  
23 non-chlorinated C<sub>2</sub> and C<sub>4</sub> compounds. The ratio between Pd-mZVI dosage, initial HCA concentration and PLA  
24 content affects the rate of H<sup>\*</sup> generation as well as the rate-determining step of the process. A pseudo-first-order  
25 equation can be applied when Pd-mZVI dosage is much higher than the theoretical stoichiometry (600 mg for  
26 [HCA]<sub>0</sub> = 5-20 mg L<sup>-1</sup>). Our results indicate that the HCA degradation mechanism includes mass transfer,  
27 sorption, surface reaction with H<sup>\*</sup>, and desorption of the product.

## 28 Keywords

29 Hexachloroethane; Pd/Fe microparticles; Iron corrosion; Physical and chemical monitoring; Dechlorination  
30 mechanism; Lactic acid polymers

## 31 1. Introduction

32 Since the first application of zero-valent iron (ZVI) as granular particles in permeable reactive barriers (PRBs)  
33 for *in situ* remediation of contaminated groundwater in the 1990s (Gillham and O'Hannesin 1994; O'Hannesin  
34 and Gillham 1998), ZVI has been the subject of widespread research to improve the reactivity, stability and  
35 transport of such particles in the subsurface environment (Zhang 2003; Crane and Scott 2012; O'Carroll et al.  
36 2013; Yan et al. 2013; Tosco et al. 2014; Liu et al. 2014b; Fu et al. 2014; Zhao et al. 2016; Reddy et al. 2016;  
37 Stefaniuk et al. 2016; Sun et al. 2016; Mu et al. 2017). The use of microscale ZVI (mZVI) particles appears to be  
38 a sustainable option, as they are less expensive and less bactericidal, and have a longer life in field experiments

39 than nanoscale ZVI (nZVI) particles (Lee et al. 2008; Comba et al. 2011; Noubactep et al. 2012; Velimirovic et  
40 al. 2012, 2013a, 2018). However, irrespective of their size, iron particles have a low electron efficiency toward  
41 contaminants and react mainly with water to produce  $\text{Fe}^{2+}$  and  $\text{H}_2$  (Schöftner et al. 2015; Fan et al. 2016; Tang et  
42 al. 2017b). It was realized that bimetallic particles, especially Pd-ZVI ones, can be used to increase the  
43 degradation rate by taking advantage of the hydrogenation reactions that generate atomic hydrogen  $\text{H}^*$  on the  
44 second metal (Lowry and Reinhard 1999; Kim and Carraway 2003; Lien and Zhang 2007; Xie and Cwiertny  
45 2013; Liu et al. 2014b). Finally, the use of a polymeric coating is essential for improving the stability, dispersion  
46 and transport of the particles in groundwater (He et al. 2007; Phenrat et al. 2008; Kaifas et al. 2014; Kocur et al.  
47 2014; Reddy et al. 2014; Han et al. 2016; Kumar et al. 2017; Fang et al. 2018).

48 Despite these improvements, the exact mechanism of contaminant removal by iron-based particles still remains  
49 unclear. The particles have a core-shell structure, with an  $\text{Fe}^0$ -core encapsulated by a thin, defective and  
50 semiconducting shell of mixed-valence  $\text{Fe}_x\text{O}_y$  iron oxides (Martin et al. 2008; Filip et al. 2014; Liu and Zhang  
51 2014; Ling et al. 2017; Bae et al. 2018). This shell is known to be the seat of all contaminant remediation  
52 processes through a combination of adsorption, reduction and co-precipitation processes (Noubactep 2008). For  
53 bimetallic particles, the presence of the second metal results in the formation of galvanic cells, Fe acting as an  
54 anode and preferentially oxidized and the second metal acting as the main cathodic site (Grittini et al. 1995; Lien  
55 and Zhang 1999), which implies that the reduction process occurs mainly on its surface. In both cases, the  
56 growth and structural evolution of the shell with time in the ZVI/ $\text{H}_2\text{O}$  system—also known as aging—generally  
57 results in a decrease of its porosity and electrical conductivity (Mu et al. 2017) and in the entrapment of the  
58 second metal (Yan et al. 2010; Ling and Zhang 2014), affecting the kinetics of iron oxidation and thus all  
59 degradation processes (Kumar et al. 2014; Liu et al. 2017). Understanding the evolution of ZVI particles and its  
60 impact on the solution chemistry is therefore crucial for evaluating their reactivity, fate and other effects.

61 Direct characterization methods, such as microscopic and spectroscopic techniques or total-iron measurements  
62 (Nurmi et al. 2005; Sun et al. 2006; Sarathy et al. 2008; Baer et al. 2008), require the recovery of solids and  
63 sample stabilization, which can be hardly feasible in the field. Such techniques are useful for characterizing the  
64 structural evolution of the iron-oxide shell, but they do not provide direct quantitative evidence of iron corrosion.  
65 Corrosion rates are commonly estimated by indirect characterization methods, especially hydrogen production  
66 measurements (Liu and Lowry 2006; Velimirovic et al. 2014), but this method is unsuitable for Pd-ZVI particles  
67 as hydrogen sorption occurs on the Pd surface (Chaplin et al. 2012). Other indirect methods focus on changes in  
68 the solution chemistry, e.g. pH and oxidation-reduction potential (ORP), due to the addition of ZVI particles and

69 the resulting reactions in the ZVI/H<sub>2</sub>O system (Yu et al. 2014). In field applications, though the complex water  
70 chemistry can alter the individual characterization ability of these methods, such indirect methods can show up  
71 evidence for ZVI-impacted zones due to the transport of iron-corrosion products, with their associated changes  
72 in biogeochemical conditions (Elliott and Zhang 2001; He et al. 2010; Wei et al. 2010, 2012, Shi et al. 2011,  
73 2015; Kocur et al. 2014). The combined use of probes appears therefore as an effective tool for understanding  
74 both the reactivity and fate of iron-based particles over short- and long-term time scales (Grieger et al. 2010; Shi  
75 et al. 2015).

76 In our previous study, we showed that the use of continuous pH and ORP measurements was effective in  
77 laboratory experiments for characterizing the degradation mechanism of hexachlorobutadiene (HCB<sub>2</sub>D) by Pd-  
78 doped ZVI microparticles (noted Pd-mZVI) suspended in dissolved lactic acid polymers and oligomers (referred  
79 to as PLA) (Rodrigues et al. 2017a). PLA is a low-cost biodegradable polymer, widely used for the  
80 denitrification of water (Wang and Chu 2016), which we selected as surface modifier to (i) Increase the viscosity  
81 of the suspension for preventing aggregation, (ii) Provide hydrophobicity on the particle surface for improving  
82 the contact with the hydrophobic pollutant, and (iii) Create acidic conditions through PLA hydrolysis and the  
83 release of organic acids for obtaining optimal conditions for the reductive dechlorination of highly chlorinated  
84 organic compounds. In addition, in field experiments, PLA acts as a slow-release source of carbon and hydrogen  
85 that can stimulate biodegradation by organohalide-respiring bacteria, to maintain reductive conditions over the  
86 long term. The efficiency of polyesters, such as polyhydroxyalkanoates (PHA), has already been proven for the  
87 bioremediation of COCs (Aulenta et al. 2008; Pierro et al. 2017). The use of ZVI-based particles with a  
88 biodegradable slow-release carbon and hydrogen source appears thus as a sustainable strategy for creating an *in*  
89 *situ* reactive zone for pollution treatment. It combines the reactivity of a short-term chemical treatment—  
90 especially for highly chlorinated and recalcitrant contaminants—with maintaining reductive conditions for long-  
91 term bioremediation, in order to prevent a potential rebound effect after the aging of iron-based particles (Baric  
92 et al. 2012; Bruton et al. 2015; Koenig et al. 2016; Kocur et al. 2016; Chronopoulou et al. 2016; Xu et al. 2017;  
93 Herrero et al. 2019).

94 The objective of our study was to elucidate the degradation mechanism of hexachloroethane (HCA, C<sub>2</sub>Cl<sub>6</sub>) using  
95 Pd-mZVI in PLA, through the indirect monitoring of iron corrosion and its associated changes in solution  
96 chemistry by means of continuous measurements of pH, ORP and conductivity. HCA is a common highly  
97 chlorinated pollutant found in soil and groundwater, with a low aqueous solubility (Rodrigues et al. 2017b). It is  
98 mainly used in the production of pyrotechnic devices and metal alloys, but it can also be a by-product of

99 fabricating lower chlorination products (Stringer and Johnston 2001). Though HCA is known to be relatively  
100 persistent in the environment (Howard 1989), it can undergo reductive dechlorination (Butler and Hayes 1998;  
101 Patterson et al. 2001; Lien and Zhang 2005; Song and Carraway 2005; Wu et al. 2014; Zhu et al. 2018). Many  
102 chlorinated intermediates can accumulate during this transformation, especially chlorinated ethanes, ethylenes  
103 and acetylenes, some of them (TCE and vinyl chloride) being classified as human carcinogens by IARC.

104 Understanding the HCA degradation mechanism is therefore important for preventing any accumulation of toxic  
105 byproducts. Experiments were first done in the absence of HCA for evaluating any changes in the Pd-  
106 mZVI/PLA/H<sub>2</sub>O system. We then investigated the effects of Pd-mZVI particles, temperature, initial HCA  
107 concentration and PLA content on the Pd-mZVI/PLA/HCA/H<sub>2</sub>O system, to provide a better insight into the  
108 degradation mechanism.

## 109 **2. Materials and methods**

### 110 *2.1. Chemicals*

111 HCA (99%) and tetrachloroethylene (PCE, 99%) were purchased from Sigma-Aldrich. A mix of chlorinated  
112 hydrocarbons in methanol (200 µg mL<sup>-1</sup>) containing chlorinated ethanes and ethylenes was obtained from  
113 Sigma-Aldrich for the preparation of standard solutions (EPA 502/524.2 VOC Mix). Stock solutions of HCA (5,  
114 10 and 20 g L<sup>-1</sup>) were prepared in HPLC-grade methanol, supplied by VWR. Deionized water was obtained from  
115 a Milli-Q water system (18.2 MΩ cm) and was degassed before any experiment with an ultrasonic bath at  
116 45 kHz, followed by N<sub>2</sub> flushing during the preparation of batch experiments to limit the introduction of O<sub>2</sub>.

117 The—partially biologically produced—Pd-doped iron microparticles (BioCAT, noted as Pd-mZVI) and the  
118 mixture of lactic acid polymers and oligomers dissolved in ethyl lactate (Dechlorem, noted as PLA) were  
119 provided by Biorem Engineering. According to the manufacturer, the particles are smaller than 10 µm with an  
120 average size of 3-5 µm, palladium representing 0.1-2 wt% of the particles. The specific surface area, measured  
121 with the BET-N<sub>2</sub> adsorption method (BELSORP-max, MicrotracBEL, Japan), was less than 1 m<sup>2</sup> g<sup>-1</sup>. The  
122 suspension of Pd-mZVI in PLA was prepared before any experiments by manual mixing of the corresponding  
123 amounts of PLA and Pd-mZVI.

124 For the system without HCA, the experiments were also performed with nZVI particles (NANOFER STAR,  
125 obtained from Nano Iron), and the results are presented in the Supplementary data.

126 2.2. *Batch experiments*

127 Batch experiments were conducted in a 1 L cylindrical Pyrex double-walled water-jacketed reactor, equipped  
128 with a mechanical-propeller stirring rod (at 300 rpm). The reactor head has hermetic ports for installing the  
129 electrodes, for the introduction of the reactant and for sampling. 1 mL of the appropriate stock solution was  
130 injected into the reactor filled with degassed deionized water with initial zero-headspace conditions. Reaction  
131 was initiated by introducing the Pd-mZVI suspension in PLA, and 3 mL aliquots were collected at selected  
132 times. The reduction was stopped by separating the particles with powerful magnets. 1 mL of the supernatant  
133 aqueous phase without particles was collected and diluted (1:10) with degassed pure water into 20 mL headspace  
134 vials equipped with a PTFE septum. The prepared samples were finally stocked at 4 °C and analysed within 24  
135 hours.

136 2.3. *Analytical methods*

137 The bimetallic microparticles were characterized before any reaction by scanning electron microscopy coupled  
138 to energy dispersive X-ray spectrometry (SEM/EDS), X-ray diffraction (XRD) and X-ray photoelectron  
139 spectroscopy (XPS). SEM/EDS images were obtained with a Phenom XL microscope (Fondis Bioritech)  
140 operating at 15 kV. XRD analyses were performed with a D8 Advance diffractometer (Bruker) with a CuK $\alpha$   
141 source ( $\lambda = 1.5406 \text{ \AA}$ ) at an accelerating voltage of 40 kV and emission current of 40 mA. Samples were scans  
142 from 4 to 90°  $2\theta$  at 0.03°  $2\theta \text{ s}^{-1}$ . XPS analyses were performed with a K-Alpha+ spectrometer (ThermoFisher  
143 Scientific) equipped with a Al anode generating Al K $\alpha$  X-ray radiation. Samples were analysed at Fe 2p, Pd 3d,  
144 C 1s, O 1s, N 1s and Si 2p regions after survey scans.

145 Analysis of HCA and its degradation products was performed by gas chromatography (GC/FID) using a Varian  
146 CP-3800 equipped with a DB-624 column (30 m x 0.32 i.d., with a 1.80  $\mu\text{m}$  film thickness). Helium was chosen  
147 as carrier gas at a 1.2 mL min $^{-1}$  flowrate. Samples were heated at 80 °C for 30 min, and 200  $\mu\text{L}$  of the headspace  
148 gas was withdrawn by a gas-tight syringe and introduced in the injector chamber at 250 °C (1:25 split ratio). The  
149 oven was maintained at 35 °C for 5 min, and then ramped up to 245 °C at 10 °C min $^{-1}$  with a hold for 10 min at  
150 this final temperature. The FID temperature was maintained at 300 °C, and He was used as carrier gas at a  
151 flowrate of 30 mL min $^{-1}$ . Combustion in the FID was carried out with H $_2$  (30 mL min $^{-1}$ ) and air (300 mL min $^{-1}$ ).  
152 Seven reference standards of chlorinated hydrocarbons, ranging from 50 to 5000  $\mu\text{g L}^{-1}$ , were periodically  
153 prepared and analysed to ensure the proper quantification of the samples. The qualitative production of non-  
154 chlorinated hydrocarbons is also provided in Supplementary data.



155 The Pd-mZVI corrosion was monitored by measuring changes in pH, ORP and conductivity with a multi-  
 156 parameter tester (Heitlab MPC 350, Heito) and recorded every 12 s using a Keithley 2700 data acquisition  
 157 system controlled via KickStart software. The pH was measured with a glass electrode (Radiometer Analytical  
 158 pHC3005-8, Hach), calibrated before each experiment with commercial buffer solutions (pH 7 and 4). The  
 159 oxidation-reduction potential (ORP) of the solution was measured with a platinum disc electrode (Radiometer  
 160 Analytical XM150, Hach) with respect to a mercury-mercurous sulphate reference electrode (MMSE, Ametek  
 161 SI). ORP values were then converted and reported with respect to the standard hydrogen electrode (SHE) by  
 162 adding 640 mV (saturated K<sub>2</sub>SO<sub>4</sub> solution). Conductivity was measured with a 2-pole conductivity cell (Tacussel  
 163 XE 150) and calibrated before each experiment with a commercial buffer solution (1413 μS cm<sup>-1</sup> at 25 °C). All  
 164 electrodes were placed in the aqueous solution at about one third of the reactor.

165 In a non-buffered system (Bae and Hanna 2015), the evolution of pH is a good indicator of iron corrosion as H<sup>+</sup>  
 166 is directly implied in the reaction (Eq. 1).



167 Eq. (1) is the result of iron oxidation in Fe<sup>2+</sup> and H<sup>+</sup> reduction in H<sub>2</sub>. The hydrogen evolution reaction (HER)  
 168 occurs both on the oxide shell and on Pd. Because of the difference in the standard redox potential, Pd acts as the  
 169 preferential cathodic site in the system, and the reduction of H<sup>+</sup> in H<sub>2</sub> occurs in a two-step process (Eqs. 2-3).



170 The formation of atomic hydrogen H<sup>\*</sup> on Pd is of crucial importance as adsorbed H<sup>\*</sup> (H<sub>ads</sub><sup>\*</sup>) is the only active  
 171 hydrogen species in catalytic hydrodechlorination reactions (Jiang et al. 2017; He et al. 2018; Liu et al. 2018).  
 172 The cumulative H<sup>+</sup> consumption, or the total generated H<sup>\*</sup> yield, can be calculated considering the reduction of  
 173 H<sup>+</sup> to H<sup>\*</sup> and the dissociation of H<sub>2</sub>O into H<sup>+</sup> before its reduction to H<sup>\*</sup> (Jiang et al. 2018), as indicated in the  
 174 Supplementary data (Fig. S3).

175 Measurements of the oxidation-reduction potential (ORP) provide information on the composition and changes  
 176 in the physico-chemistry of the solution. In the presence of ZVI particles, ORP values are mainly dependent  
 177 upon iron-species couples (Shi et al. 2011) and the H<sup>+</sup>/H<sub>2</sub> redox couple, because of the affinity of Pt (the sensing

178 probe) to hydrogen adsorption (Papaderakis et al. 2017). Finally, conductivity is an indicator of the ionic content  
179 in solution. The conductivity of the solution can be calculated by the equation below (Eq. 4):

$$\sigma = \sum_i \lambda_i z_i C_i \quad (\text{Eq. 4})$$

180 where  $\sigma$  is the conductivity ( $\text{S m}^{-1}$ ),  $\lambda_i$  the molar ionic conductivity of species  $i$  ( $\text{S m}^2 \text{mol}^{-1}$ ),  $z_i$  the electrical  
181 charge of species  $i$  and  $C_i$  the concentration of species  $i$  ( $\text{mol m}^{-3}$ ). Considering iron corrosion and HCA  
182 dechlorination, the main ionic species that can influence the conductivity are  $\text{H}^+$  (at  $25^\circ\text{C}$ ,  $\lambda_{\text{H}^+}^\circ = 349.8 \text{ S cm}^2$   
183  $\text{mol}^{-1}$ ),  $\text{OH}^-$  ( $\lambda_{\text{OH}^-}^\circ = 198 \text{ S cm}^2 \text{mol}^{-1}$ ),  $\text{Fe}^{2+}$  ( $\lambda_{1/2\text{Fe}^{2+}}^\circ = 54 \text{ S cm}^2 \text{mol}^{-1}$ ),  $\text{Fe}^{3+}$  ( $\lambda_{1/3\text{Fe}^{3+}}^\circ = 68 \text{ S cm}^2 \text{mol}^{-1}$ ),  $\text{Cl}^-$  ( $\lambda_{\text{Cl}^-}^\circ$   
184  $= 76 \text{ S cm}^2 \text{mol}^{-1}$ ), and the ionic species resulting from the introduction and hydrolysis of PLA. The decrease in  
185  $\text{H}^+$  content due to iron corrosion is responsible for a decrease in conductivity, whereas an increase in the contents  
186 of other ionic species causes an increase in conductivity.

### 187 3. Results and discussion

#### 188 3.1. Characterization of Pd-mZVI particles

189 The characterization of the Pd-mZVI particles before reaction is shown in Fig. 1 and Fig S1. On Fig. 1a, it is  
190 shown that the smallest particles were spherical, with a diameter of 2-3  $\mu\text{m}$ . Larger particles with a diameter of  
191 about 10  $\mu\text{m}$  were also observed (Fig. S1a). On Fig. S1b, the largest particles show the porous structure of the  
192 external layer. In addition, EDS analysis reveals that some of the particles have a high carbon content with traces  
193 of silicium and phosphorus, which could originate from the biomass used during the bioreductive deposition of  
194 palladium nanoparticles (De Windt et al. 2005; Dien et al. 2013).

195 Fig. 1b shows the patterns of the Pd-mZVI particles. The peaks at  $44.7^\circ$ ,  $65.1^\circ$  and  $82.3^\circ$ , respectively, can be  
196 indexed to the planes (110), (200) and (211) of Fe cubic crystal structure (JCPDS 06-0696), and the peaks at  
197  $40.3^\circ$ ,  $46.9^\circ$  and  $68.5^\circ$ , respectively, correspond to the planes (111), (200) and (220) of face centered cubic  
198 crystal structure of Pd (the peak at  $82.3^\circ$  can also be attributed in part to the plane (311)) (JCPDS 46-1043).  
199 However, there is no indication of crystalline phases of iron oxide, or only in very small fractions, in contrary to  
200 the pattern of nZVI particles for which the diffraction peaks corresponding to magnetite or maghemite were  
201 observed (Fig. S2a). Figs 1c, d and e show the XPS spectra of the Pd-mZVI particles. The survey scan from 0 to  
202 1100 eV indicates the presence of Fe, Pd, C, O, N and Si on the surface of the particles (Fig. 2a). As indicated by  
203 the low signal intensities between 700 and 730 eV (Fig. 2b), the presence of Fe on the surface of the particles is  
204 very limited, in comparison to nZVI particles for which the XPS spectra indicates the presence of metallic iron

205 (Fe<sup>0</sup>) and oxidized iron (Fe<sup>III</sup>) on its surface and near-surface (Fig. S2). The particles present four peaks between  
206 332 and 346 eV, named A1, B1, A2 and B2 (Fig. 2c). The two peaks A1 and A2, with binding energies of 335.4  
207 and 340.7 eV respectively, match with the 3d<sub>5/2</sub> and 3d<sub>3/2</sub> of metallic Pd (Muftikian et al. 1996; Yan et al. 2010),  
208 and the two peaks B1 and B2, with binding energies of 338.1 and 343.4 eV respectively, match with the 3d<sub>5/2</sub> and  
209 3d<sub>3/2</sub> of oxidized Pd (Voogt et al. 1996). The results indicate that, for Pd-mZVI particles, the core is mainly  
210 composed of Fe<sup>0</sup>, while the external surface of the particles is composed of iron oxides, carbon, silica, and  
211 palladium, the latter being required for H<sup>\*</sup> generation for hydrodechlorination on the surface.

### 212 3.2. Investigation of the Pd-mZVI/PLA/H<sub>2</sub>O system

213 Before considering HCA degradation, two experiments were performed without HCA at 25 °C in the presence of  
214 600 mg of Pd-mZVI and 850 or 3400 mg of PLA. This was to investigate the influence of PLA on the corrosion  
215 kinetics of Pd-mZVI and to understand how to interpret the evolution of pH, ORP and conductivity (Fig. 2).

216 With 850 mg of PLA, the introduction of PLA in solution resulted in an initial drop of pH to 2.65 (Fig. 2a, with  
217 pK<sub>a</sub> of lactic acid = 3.86 at 20 °C) and a first increase of conductivity to 350 μS cm<sup>-1</sup> (Fig. 2d). Initially, the ORP  
218 values were fixed by the Fe(III)/Fe(II) redox couple (Figs. 2b and c) that result from the initial partial breaking  
219 of the iron oxide shell under acidic conditions (Sarathy et al. 2008; Tang et al. 2017a). This agrees with the  
220 initial decrease and stabilization of pH as Fe<sup>3+</sup> acts as a weak Brønsted acid (Shih et al. 2011), as indicated in Eq.  
221 5.



222 After 420 minutes, the pH increased from 2.65 to 6.15, and the rate of H<sup>+</sup> consumption is not linear but decreases  
223 with time, as shown by the cumulative H<sup>+</sup> consumption (Fig. S3). After an initial decrease, the conductivity  
224 stabilized at a minimum value of 195 μS cm<sup>-1</sup> after 100 min. The decrease in H<sup>+</sup> content was therefore  
225 compensated by an increase in other ionic-species contents, especially soluble Fe<sup>2+</sup> and Fe<sup>3+</sup>. After that,  
226 conductivity slowly increased to 230 μS cm<sup>-1</sup> at 420 min.

227 According to the Nernst equation of the Fe(III)/Fe(II) redox couple, an increase in Fe<sup>2+</sup> content resulting from  
228 iron corrosion (Eq. 1) causes a decrease in ORP values in the first minutes. Then, ORP drops from positive to  
229 negative values (Fig. 2b), which indicates a change in the main redox couple in the system. As shown on Fig. 2c,  
230 this change is well correlated with the theoretical evolution of the H<sup>+</sup>/H<sub>2</sub> redox couple with pH. Hence, the  
231 monitoring of ORP is a good indicator for the formation and accumulation of H<sub>2</sub> in the system. A similar  
232 behaviour was observed for the aqueous corrosion of nZVI particles in PLA (Fig. S4), confirming that the

233 changes in solution chemistry are well related to the particles. However, all phenomena accelerated when using  
234 nZVI particles. The pH increased from 2.75 to 6.15 in less than 60 min, resulting in a more rapid initial decrease  
235 in both ORP and conductivity. This acceleration is probably related to the difference in specific surface area ( $a_{s,nZVI,BET} = 15.5 \text{ m}^2 \text{ g}^{-1}$ ) and in the cathode/anode ratio. The nZVI particles thus show a much faster corrosion rate  
236 than Pd-mZVI particles, the latter having a longer reactive lifetime.

238 The increase in PLA content from 850 to 3 400 mg led to a decrease in initial pH (Fig. 2a) due to PLA  
239 hydrolysis, resulting in an increase in initial conductivity (Fig. 2d). Similar changes of pH and ORP were  
240 observed, but with a time delay; the decrease and stabilization of pH values (Fig. 2a) and the fixing of ORP by  
241 the Fe(III)/Fe(II) redox couple (Figs. 2b, c) were observed during 40 min. After that, the pH sharply increased  
242 reflecting a more rapid decrease in conductivity (Fig. 2d), and the change of ORP from the Fe(III)/Fe(II) to the  
243  $\text{H}^+/\text{H}_2$  redox couple occurred shortly after. Compared with the experiment conducted with 850 mg of PLA, this  
244 evolution of the solution chemistry thus suggests that, despite an initial decrease in pH, iron corrosion is slow  
245 from 0 to 40 min, becoming important only after that. The polymeric coating can alter the reactivity of iron-  
246 based particles due to (i) the blocking of reactive sites and (ii) the inhibition of mass transfer to the surface due to  
247 the formation of trains and loops (Phenrat et al. 2009). Increasing the PLA content results in blocking of the  
248 reactive cathodic sites and the creation of an extensive polymer layer on the surface. Iron corrosion thus appears  
249 to be initially cathodically controlled by  $\text{H}^+$  mass transport to the Pd surface, the effect being more pronounced  
250 when the PLA content is increased. Increasing the  $\text{H}^+$  content at the interface causes an increase in corrosion  
251 rate, resulting in the saturation of Pd and the later recombination of  $\text{H}^*$  into  $\text{H}_2$ . A schematic illustration of the  
252 main results obtained in this section is proposed on Fig. 3.

253 Continuous pH, ORP and conductivity measurements allowed monitoring the consumption of  $\text{H}^+$ , mainly related  
254 to iron corrosion, and the production/accumulation of  $\text{H}_2$  in the system according to the E-pH diagram.

### 255 3.3. Investigation of the Pd-mZVI/PLA/HCA/ $\text{H}_2\text{O}$ system

#### 256 3.3.1. Effects of Pd-mZVI dosage

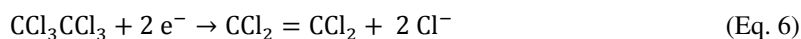
257 The effect of Pd-mZVI dosage was investigated with 150, 375 and 600 mg at 25 °C with 850 mg of PLA and  
258  $10 \text{ mg L}^{-1}$  of HCA (Fig. 4). It is important to note that the theoretical stoichiometric requirement is  $1.42 \text{ g Fe}^0/\text{g}$   
259 of HCA for its complete reduction to ethane. HCA completely disappears in less than 120 min with 600 mg of  
260 Pd-mZVI, while the degradation remains incomplete after 420 min with 150 and 375 mg (Fig. 4a). An increase  
261 in Pd-mZVI dosage results in more active sites for  $\text{H}^+$  reduction and  $\text{H}^*$  generation (cathodic sites), as confirmed

262 by the more rapid increase in pH (Fig. 4b). As shown on Figs. 4d and e, ORP remained fixed by the  
263 Fe(III)/Fe(II) redox couple with 150 and 375 mg, while the change from Fe(III)/Fe(II) to H<sup>+</sup>/H<sub>2</sub> was observed  
264 with 600 mg. This result agrees with the more rapid and greater production of H<sub>2</sub>. With 150 and 375 mg of Pd-  
265 mZVI, the conductivity decreases during the 420 min of reaction time (Fig. 4f). This decrease is observed during  
266 the first 90 min with 600 mg of Pd-mZVI. As H<sup>+</sup> is the major contributor to conductivity under strong acidic  
267 conditions, this variation can be explained by a decrease in H<sup>+</sup> content due to iron corrosion.

268 HCA reduction results in the formation and accumulation of PCE (C<sub>2</sub>Cl<sub>4</sub>) as the only chlorinated intermediate  
269 (Fig. 4c), in agreement with the dihalo-elimination pathway observed in earlier studies with ZVI-based particles  
270 (Lien and Zhang 2005; Song and Carraway 2005; Wu et al. 2014). However, our results showed that the initial  
271 disappearance of HCA was not directly related to PCE production, as a 10-min shift was observed for PCE  
272 production irrespective of the amount of particles. This delay may indicate that HCA degradation initially  
273 involves nonreductive sorption on the Pd-mZVI/PLA/H<sub>2</sub>O system, which is generally linked to the carbon  
274 content on the particle surfaces (Lin and Lo 2005; Velimirovic et al. 2013b). In addition, this induction period  
275 could be caused by the absence of active hydrogen species (H<sub>ads</sub><sup>\*</sup>) on the Pd surface, as He et al. (2018)  
276 suggested that the dechlorination process on Pd particles requires first their saturation by H<sup>\*</sup> (formation of  
277 palladium hydride) before any dechlorination reaction.

278 With 600 mg of Pd-mZVI, the change from positive to negative ORP values occurs after 100 min (Fig. 4d)  
279 whereas it occurs after only 35 min in the absence of HCA (Fig. 2b), showing that H<sup>\*</sup> is consumed during  
280 dechlorination. This change is observed only when the PCE concentration becomes low, indicating that H<sup>\*</sup> is the  
281 main reductant for both HCA and PCE degradation. However, the degradation mechanism seems different for  
282 both compounds. HCA reduction to PCE (Eq. 6) does not involve the addition of hydrogen in the molecule;  
283 atomic hydrogen acts therefore only as an electron donor. Even if this result seems to disagree with the increase  
284 in pH, it is important to note that iron particles have a very low electron efficiency toward contaminants, i.e.  
285 most parts of iron react with water (Schöftner et al. 2015; Fan et al. 2016; Tang et al. 2017b). PCE reduction  
286 results in the formation of ethane, ethylene and C<sub>4</sub> compounds (Fig. S6), without accumulation of chlorinated  
287 intermediates in solution. This result was confirmed by GC/MS measurements with lower quantitation limits  
288 (0.1-1 µg L<sup>-1</sup> depending on the compound). The production of C<sub>4</sub> compounds indicates that coupling reactions  
289 occur during the reaction. Hence, PCE reduction first results in the formation of C<sub>2</sub> surface complexes, with the

290 loss of chloride ions due to the breaking of C-Cl bonds on the catalyst (Sriwatanapongse et al. 2006; Heck et al.  
 291 2008), followed by progressive hydrogenation and/or coupling reactions between C<sub>2</sub> fragments (Eqs. 7-10).



292 With 600 mg of Pd-mZVI, the small increase in ORP values (Fig. 4d)—causing a gap in the H<sup>+</sup>/H<sub>2</sub> redox couple  
 293 theoretical values observed after 120 min (Fig. 4e)—is caused by the loss of H<sub>2</sub> during sampling, as ORP  
 294 remains well fixed by the H<sup>+</sup>/H<sub>2</sub> redox couple without opening of the reactor (Fig. 2c). The effect is more  
 295 pronounced for the penultimate sampling at 330 min because of the decrease in H<sup>+</sup> content and the rate of iron  
 296 corrosion. The effect is even more pronounced with nZVI particles (Fig. S4), where a decrease in pH is observed  
 297 after 80 min associated with a progressive increase in ORP every time the reactor is opened. These results  
 298 indicate a consumption of OH<sup>-</sup> and the formation of iron oxy-hydroxides on the surface of nZVI particles such as  
 299 lepidocrocite γ-FeOOH, because of the possible introduction of dissolved O<sub>2</sub> (Greenlee et al. 2012; Liu et al.  
 300 2014a), as well as of ferrihydrite because of the presence of lactate ions (Sabot et al. 2007).

301 Zero-order, pseudo-first-order and second-order reactions were envisaged for fitting the experimental data. With  
 302 150 and 375 mg of Pd-mZVI, none of them resulted in a correct representation of HCA degradation (see Table 1  
 303 for the results of pseudo-first-order equations). In these cases, a two-compartment model based on first-order  
 304 equations (Eq. 11) fits well with the experimental data obtained (Fig. S6), suggesting that two different reaction  
 305 mechanisms explain the disappearance of HCA (Rodrigues et al. 2017a; Kim et al. 2018).

$$\frac{C}{C_0} = \alpha e^{-k_a t} + (1 - \alpha) e^{-k_c t} \quad (\text{Eq. 11})$$

306 where C<sub>0</sub> is the initial pollutant concentration, C is the pollutant concentration at time t (min), k<sub>a</sub> and k<sub>c</sub> are  
 307 respectively the rate constants for adsorption and chemical degradation, α represents the weight value for  
 308 sorption, and 1-α represents the weight value for chemical degradation.

309 With 600 mg of Pd-mZVI, the production of atomic hydrogen H<sup>\*</sup> on the Pd surface is more important due to  
 310 increased H<sup>+</sup> consumption. The rate-determining step then moves progressively from H<sup>\*</sup> production to hydro-

311 dechlorination by increasing Pd-mZVI dosage, which can explain the validity of the pseudo-first-order model  
312 (Eq. 12):

$$\frac{C}{C_0} = e^{-k_{\text{obs}}t} \quad (\text{Eq. 12})$$

313 where  $C$  is the concentration ( $\text{mg L}^{-1}$ ) at time  $t$  (min),  $C_0$  is the initial concentration ( $\text{mg L}^{-1}$ ) and  $k_{\text{obs}}$  is the rate  
314 constant ( $\text{min}^{-1}$ ).

315 In the following section, we focus on the use of 600 mg of Pd-mZVI in order to observe as much variation as  
316 possible in the different experimental parameters for a better understanding of the HCA degradation mechanism.

### 317 3.3.2. *Effects of temperature*

318 The effect of temperature was investigated at 12, 25 and 35 °C with 600 mg of Pd-mZVI, 850 mg of PLA and  
319 10  $\text{mg L}^{-1}$  of HCA (Fig. 5). As already observed in our previous study (Rodrigues et al. 2017a), the increase in  
320 temperature results in a decrease in the initial pH due to a change in the rate of PLA hydrolysis. Results show  
321 that HCA degradation is incomplete at 12 °C after 420 min (Fig. 5a). During this period, the pH increases from  
322 2.94 to 3.48 (Fig. 5b), and only a decrease in conductivity with time from 390 to 225  $\mu\text{S cm}^{-1}$  is observed  
323 (Fig. 5f), indicating that iron corrosion is slow. At 35 °C, the HCA has completely disappeared after about  
324 60 min, more rapidly than at 25 °C (Fig. 5a), and PCE accumulates at a lower rate and disappears more rapidly at  
325 35 °C (Fig. 5c). In addition to the increase in the number of high-energy collisions and in the mobility of the  
326 pollutant, the rise in temperature from 12 to 35 °C increases  $\text{H}^+$  consumption (Fig. S3). Direct comparison of the  
327 evolution of conductivity is more difficult here as the molar conductivity of each species is different at each  
328 temperature, but the results confirm that iron corrosion is more rapid when the temperature increases (Fig. 5f).  
329 The constant increase in HCA degradation rate with temperature (Table 1) can then be explained by the more  
330 rapid production of atomic hydrogen on the Pd surface (He and Zhao 2008).

331 This agrees with the evolution in ORP values over time. At 12 °C, ORP is stable for 100 min and only a small  
332 decrease is observed afterwards (Fig. 5d), indicating an increase in  $\text{Fe}^{2+}$  content in the solution. The ORP does  
333 not decrease to the  $\text{H}^+/\text{H}_2$  redox couple values because of the slow production of atomic hydrogen and its  
334 subsequent reaction with HCA. Conversely, the accumulation of  $\text{H}_2$ , according to ORP measurements (Fig. 5d),  
335 is more rapid at 35 °C than at 25 °C, as both HCA and PCE degradation occur more rapidly. Consequently, the  
336 decrease in  $\text{H}^+$  consumption under less acidic conditions ( $\text{pH} > 5$ ) is observed earlier at 35 °C. After the last  
337 opening of the reactor at 330 min, the ORP becomes positive, indicating that the  $\text{H}^+/\text{H}_2$  redox couple is no longer

338 the main contributor to the overall ORP value (Figs. 5d and e). Also, the small decrease in pH observed could  
 339 indicate an OH<sup>-</sup> consumption related to the formation of iron oxy-hydroxides on the particle surfaces. Thus, even  
 340 if the temperature increase is favourable for HCA degradation, the reactive lifetime of the particles and the  
 341 electron efficiency are strongly impacted. We thus focused on the use of  $T = 25\text{ }^{\circ}\text{C}$  for the subsequent  
 342 experiments.

343 Considering the pseudo-first-order model, the Arrhenius equation was used for establishing the relation between  
 344 the rate constant and the temperature (Eq. 13).

$$\ln k_{\text{obs}} = \ln A - \frac{E_a}{RT} \quad (\text{Eq. 13})$$

345 where  $k_{\text{obs}}$  is the constant rate ( $\text{min}^{-1}$ ),  $A$  is the pre-exponential factor ( $\text{min}^{-1}$ ),  $E_a$  is the activation energy ( $\text{J mol}^{-1}$ ),  
 346  $R$  is the universal gas constant and  $T$  is the absolute temperature (K). An almost equivalent relationship, the  
 347 Eyring equation, can be used by following the transition state theory (Eq. 14).

$$k_{\text{obs}} = \frac{k_B T}{h} \exp\left(\frac{-\Delta^\ddagger G^\circ}{RT}\right) \quad (\text{Eq. 14})$$

348 where  $k_B$  is the Boltzmann constant ( $1.381 \cdot 10^{-23} \text{ J K}^{-1}$ ),  $h$  is the Planck constant ( $6.626 \cdot 10^{-34} \text{ J s}$ ) and  $\Delta^\ddagger G^\circ$  is the  
 349 Gibbs energy of activation ( $\text{J mol}^{-1}$ ). The relation can be linearized as Eq. 15:

$$\ln\left(\frac{k_{\text{obs}}}{T}\right) = \frac{-\Delta^\ddagger H^\circ}{R} \cdot \frac{1}{T} + \ln\left(\frac{k_B}{h}\right) + \frac{\Delta^\ddagger S^\circ}{R} \quad (\text{Eq. 15})$$

350 where  $\Delta^\ddagger H^\circ$  is the standard enthalpy of activation ( $\text{J mol}^{-1}$ ) and  $\Delta^\ddagger S^\circ$  is the standard entropy of activation ( $\text{J mol}^{-1}$   
 351  $\cdot \text{K}^{-1}$ ).

352 Results obtained from the Arrhenius plot are  $E_a = 106.5 \text{ kJ mol}^{-1}$  and  $A = 1.21 \cdot 10^{17} \text{ min}^{-1}$  ( $R^2 = 0.982$ , Fig. S8a).

353 The elevated activation energy indicates that, with these experimental parameters, the overall reaction is  
 354 controlled by the reaction on the particle surfaces (Pilling and Seakins 1995). Results obtained from the Eyring  
 355 plot are  $\Delta^\ddagger H^\circ = 104.0 \text{ kJ mol}^{-1}$  and  $\Delta^\ddagger S^\circ = 39.8 \text{ J mol}^{-1} \text{ K}^{-1}$  ( $R^2 = 0.981$ , Fig. S8b). The positive value for the  
 356 activation entropy indicates that the reaction is favourable and that the activated complex is loosely bound on the  
 357 surface of the particles, which agrees with the formation and desorption of PCE as a reaction intermediate. Based  
 358 on previous studies (Butler and Hayes 1998; Patterson et al. 2001; Song and Carraway 2005; Huang et al. 2012;  
 359 Pizarro et al. 2018), the activated complex is suspected to be the pentachloroethyl radical (Eqs. 16-17).





### 360 3.3.3. *Effects of HCA initial concentration*

361 The effect of the initial concentration was investigated at three HCA initial concentrations—5, 10 and 20 mg L<sup>-1</sup>—at 25 °C with 600 mg of Pd-mZVI and 850 mg of PLA (Fig. 6). A change in initial concentration of the  
362 substrate has no influence on the degradation pathways, with the production of PCE and its subsequent reduction  
363 to ethane, ethylene and C<sub>4</sub> compounds (Fig. S9). HCA degradation-rate constants are very similar when the  
364 initial concentration increases from 5 mg L<sup>-1</sup> (*k*<sub>obs</sub> = 0.036 min<sup>-1</sup>) to 10 mg L<sup>-1</sup> (*k*<sub>obs</sub> = 0.035 min<sup>-1</sup>, see Table 1).  
365 As the evolution of H<sup>+</sup> content is quite different at both concentrations (Figs. 6b and S2), the rate-determining  
366 step cannot be attributed to H<sup>\*</sup> production, but rather to HCA dechlorination.

368 An increase in HCA content to 20 mg L<sup>-1</sup> results in a decrease in the degradation rate constant (*k*<sub>obs</sub> = 0.010 min<sup>-1</sup>), and PCE accumulates over a longer time, but in a similar proportion as obtained with lower initial  
369 concentrations (Fig. 6c). As indicated by the pH evolution (Fig. 6b) and cumulative H<sup>+</sup> consumption (Fig. S3),  
370 the production of H<sup>\*</sup> is less rapid with 20 mg L<sup>-1</sup>, whereas the degradation requires twice as much atomic  
371 hydrogen. As observed in Figs. 6d and e, the ORP value remains positive and is not fixed by the H<sup>+</sup>/H<sub>2</sub> redox  
372 couple during the 420 min of the experiment. As shown on Fig. S10, the drop in ORP values is observed only  
373 after the complete hydrodechlorination of PCE. So, as long as dechlorination occurs, the most important fraction  
374 of H<sup>\*</sup><sub>ads</sub> available on Pd is consumed, which prevents its recombination into H<sub>2</sub> and its subsequent desorption.  
375 Therefore, even if the degradation rate constant is lower, a low iron/pollutant ratio will limit the loss of active  
376 hydrogen species. This result is comparable to that obtained by decreasing the amount of Pd-mZVI, where a  
377 similar evolution of conductivity with time is observed (Fig. 6f). Hence, for higher HCA initial concentrations  
378 (>20 mg L<sup>-1</sup>) with 600 mg of Pd-mZVI, the reaction may be limited by the production of H<sup>\*</sup> and not by surface-  
379 reaction kinetics.

381 In the following section, we thus focus on the use of 10 mg L<sup>-1</sup> as the initial HCA concentration.

### 382 3.3.4. *Effects of PLA content*

383 The effect of the PLA content was investigated for three initial contents—850, 1700 and 3400 mg—at 25 °C  
384 with 600 mg Pd-mZVI and 10 mg L<sup>-1</sup> HCA (Fig. 7). The increase in PLA content results in a decrease in HCA  
385 degradation rate constants, from 0.035 min<sup>-1</sup> with 850 mg to 0.025 min<sup>-1</sup> at 3400 mg (Table 1), in agreement with

386 the later production and accumulation of PCE (Fig. 7c). With 3400 mg, more than 40% of HCA disappears in the  
387 first 10 min, which indicates a more important phase transfer from water to PLA (sorption). As no PCE  
388 production is observed during this time, HCA accumulates near the surface of the particles. Compared to the  
389 experiment run in the Pd-mZVI/PLA/H<sub>2</sub>O system (Fig. 2), the evolution of pH, ORP and conductivity follows  
390 the same qualitative trend (Figs. 7b, d and f), although H<sup>+</sup> consumption is less important in the first minutes  
391 (Fig. S3) and the change from a Fe(III)/Fe(II) to a H<sup>+</sup>/H<sub>2</sub> redox couple occurs much later.

392 In the Pd-mZVI/PLA/H<sub>2</sub>O system, the reductive dechlorination process requires an intimate contact between  
393 pollutant and particle surface. However, as mentioned before, the increase in polymeric coating can result in a  
394 high coverage rate of the particles (site blocking) and the development of an extended layer composed of loops  
395 and tails (Zhu et al. 2008; Phenrat et al. 2009; Bhattacharjee et al. 2016; Louie et al. 2016). With 1700 mg of  
396 PLA, the lower HCA rate constant can be attributed to higher number of sites blocked by the polymeric coating  
397 and to a low production of atomic hydrogen in the first minutes. After the initial decrease and stabilization of pH  
398 (Fig. 7b), the strong acidic conditions accelerate the rate of H<sup>+</sup> consumption (Fig. S3), which results in a more  
399 rapid production of H<sup>\*</sup>. As a consequence, PCE degradation occurs rapidly. With 3400 mg of PLA, the  
400 development of loops and tails on the particle surfaces will impede HCA mass transport to the surface of the  
401 particles, the accumulation of HCA in turn impeding H<sup>+</sup> mass transport, which explains the decrease in  
402 degradation rate. In addition, the accumulation of H<sub>2</sub> bubbles around the particles can result in the covering of  
403 reactive sites and the deactivation of the catalyst (Graham and Jovanovic 1999; Wang et al. 2009), leading to a  
404 further decrease in the degradation rate (Huang et al. 2016).

405 Even if the degradation rates decrease with increasing PLA content, the reactive lifetime of the particles is  
406 extended thanks to the formation of iron lactate complexes and the maintenance of acidic conditions, which  
407 prevent the rapid formation of any passive layer on the surface of the particles (Rodrigues et al. 2017a) as Fe<sup>3+</sup>  
408 and Fe<sup>2+</sup> are more soluble under acidic conditions, and thus the rapid enclosure of Pd (Yan et al. 2010; Ling and  
409 Zhang 2014).

410 As shown in the previous experiments, for a given initial HCA concentration, an increase in Pd-mZVI dosage  
411 causes an increase in the HCA degradation rate, but a major part of the H<sup>\*</sup> will be combined as H<sub>2</sub>, rendering it  
412 unavailable for degradation. Therefore, it appears necessary to seek a compromise between HCA degradation  
413 rate and electron efficiency. A 15:85 mass ratio of Pd-mZVI in PLA appears to be an optimal condition that

414 allows a rapid initial disappearance of the pollutant, a more controlled reactivity and the maintenance of acidic  
415 conditions, extending the reactive lifetime of the particles and preventing the formation of passive precipitates.

#### 416 3.4. HCA dechlorination mechanism

417 Figure 8 shows a summary of the main conclusions of the dechlorination mechanism. The introduction in water  
418 of a suspension of Pd-mZVI in PLA results in the partial breaking up of the initial shell (Sarathy et al. 2008;  
419 Tang et al. 2017a);  $\text{Fe}^0$  oxidizes to  $\text{Fe}^{2+}$ , and the resulting electrons flow from the iron core to Pd that acts as the  
420 main cathodic site ( $E^0_{\text{Pd}} > E^0_{\text{FeOx}} > E^0_{\text{Fe}}$ ). On the Pd surface, which is a good catalyst for hydrogenation,  $\text{H}^+$  is  
421 reduced to atomic hydrogen  $\text{H}^*$  (Volmer step), accumulating as palladium hydride (Pd-H) and as  $\text{H}^*_{\text{ads}}$ . Finally,  
422 the reaction of  $\text{H}^+$  with  $\text{H}^*_{\text{ads}}$  (Heyrovsky step), or the combination of two  $\text{H}^*_{\text{ads}}$  (Tafel step), will result in the  
423 desorption of  $\text{H}_2$  to the bulk solution (Fig. 3).

424 In the presence of HCA, the first step is mass transfer of HCA from bulk to suspension of the Pd-mZVI/PLA  
425 system. As both HCA and PLA are hydrophobic, the initial HCA disappearance is attributed to nonreductive  
426 sorption, in agreement with the absence of PCE production and the increase in initial disappearance when  
427 increasing the PLA content. The second step is the surface reaction of HCA with  $\text{H}^*$ , which results in the  
428 production and accumulation of PCE as a chlorinated by-product. The absence of other chlorinated intermediates  
429 and the production of  $\text{C}_4$  compounds suggest that PCE undergoes rapid dechlorination, because of the breaking  
430 of C-Cl bonds on the Pd surface (Sriwatanapongse et al. 2006; Heck et al. 2008) and the formation of  $\text{C}_2^\ddagger$  surface  
431 complexes. The third step is the progressive hydrogenation of  $\text{C}_2^\ddagger$  into  $\text{C}_2$  compounds, or a coupling reaction  
432 between two surface complexes into  $\text{C}_4^\ddagger$  and its progressive hydrogenation to  $\text{C}_4$  compounds. The last steps are  
433 the desorption of the products from the surface of the particles, and their transfer to the bulk solution (Fig. 8).

#### 434 3.5. Implications for environmental application

435 In addition to proposing a degradation mechanism, our study allows defining some perspectives for practical  
436 applications. The laboratory results suggest that small ( $\approx 600$  mg for  $[\text{HCA}]_0 = 5\text{-}20$  mg  $\text{L}^{-1}$ ) amounts of Pd-  
437 mZVI in PLA are sufficient for a rapid and complete pollution degradation. The use of low doses of iron  
438 particles will limit the loss of ZVI due to its spontaneous corrosion in water, as well as reducing its inhibition  
439 effects on the microbial community for *in situ* remediation (Velimirovic et al. 2015). Even if an increase in PLA  
440 content results in more acidic conditions, the effect may be less pronounced under field conditions depending on  
441 the natural buffering capacity of the aquifer. In addition, as indicated above, iron corrosion progressively results  
442 in an increase of pH to near-neutral conditions, more favourable to the growth and activity of organohalide-

443 respiring bacteria, e.g. *Dehalococcoides* strains, for biological reductive dechlorination, even if a pH decrease  
444 will affect the ability of the culture to dechlorinate (Yang et al. 2017a, b). The monitoring of pH thus is a great  
445 tool for evaluating the operating conditions for both abiotic and biotic reductive processes.

446 Interpretation of the ORP evolution should be more difficult in the field than in laboratory experiments, because  
447 of the many redox couples and bacteria in groundwater that contribute to the overall (mixed potential) ORP  
448 value (Hunting and Kampfraath 2013; Shi et al. 2015). Measuring ORP will nevertheless provide insight into the  
449 creation of reductive conditions due to H<sub>2</sub> production. In addition, the impact on ORP values of opening the  
450 reactor could mirror the influence of sampling from observation wells in the field, as ORP values are known to  
451 have a harmful effect on iron reactivity, and on the presence and activity of organohalide-respiring bacteria  
452 (Adrian and Löffler 2016). Finally, conductivity measurements should give indications on the ionic strength of  
453 groundwater. The overall data acquired during this study have shown the interest of implementing a complete  
454 multi-parametric device for the monitoring of reductive dechlorination processes in the field.

#### 455 **4. Conclusion**

456 We investigated the mechanism of HCA degradation by a suspension of Pd-mZVI particles in PLA, using  
457 indirect continuous monitoring of iron corrosion by means of measuring pH, ORP and conductivity. HCA  
458 dechlorination involves the formation and accumulation of PCE as an intermediate compound, before its  
459 subsequent reduction to non-chlorinated C<sub>2</sub> and C<sub>4</sub> compounds. The increase in Pd-mZVI dosage results in an  
460 increased HCA degradation rate due to a greater production of atomic hydrogen H<sup>\*</sup>. With 600 mg of Pd-mZVI  
461 particles, a temperature increase is favourable to HCA degradation as the production of H<sup>\*</sup> is accelerated, but at  
462 the expense of the reactive lifetime of the particles. Increasing the initial HCA concentration to 20 mg L<sup>-1</sup> leads  
463 to a decrease in the degradation rate constant. Finally, an increase in PLA content decreases the global  
464 degradation rate due to an enhanced contact between HCA and the particle surfaces that decreases the production  
465 of H<sup>\*</sup>, but the maintaining of acidic conditions can prevent the rapid formation of any passive precipitates. Our  
466 results indicate that the HCA degradation mechanism includes mass transfer, nonreductive sorption, surface  
467 reaction with H<sup>\*</sup> and desorption of the product. Combined with gas chromatography, the continuous monitoring  
468 of physical and chemical parameters of the bulk solution was proven to be a powerful tool in laboratory  
469 experiments for the indirect investigation of dechlorination mechanisms in the Pd-mZVI/PLA/H<sub>2</sub>O system.

470 **Appendix A. Supplementary data**

471 Supplementary data are associated with this article.

472 **Declaration of interest**

473 None

474 **Acknowledgements**

475 This work was supported by the French Environment and Energy Management Agency (ADEME) and the  
476 French Geological Survey (BRGM) within the framework of the AMI SILPHES project coordinated by David  
477 Cazaux (Inovyn Tavaux). The authors acknowledge Benoit Castermans (Biorem Engineering) for providing Pd-  
478 mZVI particles and PLA, Nicolas Maubec (BRGM) for performing XRD analyses, and Christian Perruchot and  
479 Philippe Decorse (ITODYS laboratory, Université Paris Diderot) for performing XPS analyses. Romain  
480 Rodrigues thanks Chérif Morcos for fruitful discussions. The authors thank the anonymous reviewers for their  
481 helpful comments and suggestions. H.M. Kluijver edited the English language of the final MS.

482 **References**

- 483 Adrian L, Löffler FE (2016) *Organohalide-Respiring Bacteria*. Springer, Berlin, Heidelberg
- 484 Aulenta F, Fuoco M, Canosa A, Papini MP, Majone M (2008) Use of poly- $\beta$ -hydroxy-butyrate as a slow-release  
485 electron donor for the microbial reductive dechlorination of TCE. *Water Sci Technol* 57:921. doi:  
486 10.2166/wst.2008.073
- 487 Bae S, Collins RN, Waite TD, Hanna K (2018) Advances in surface passivation of nanoscale zerovalent iron  
488 (NZVI): A critical review. *Environ Sci Technol* acs.est.8b01734. doi: 10.1021/acs.est.8b01734
- 489 Bae S, Hanna K (2015) Reactivity of nanoscale zero-valent iron in unbuffered systems: Effect of pH and Fe(II)  
490 dissolution. *Environ Sci Technol* 49:10536–10543. doi: 10.1021/acs.est.5b01298
- 491 Baer DR, Amonette JE, Engelhard MH, Gaspar DJ, Karakoti AS, Kuchibhatla S, Nachimuthu P, Nurmi JT,  
492 Qiang Y, Sarathy V, Seal S, Sharma A, Tratnyek PG, Wang C-M (2008) Characterization challenges for  
493 nanomaterials. *Surf Interface Anal* 40:529–537. doi: 10.1002/sia.2726
- 494 Baric M, Majone M, Beccari M, Papini MP (2012) Coupling of polyhydroxybutyrate (PHB) and zero valent iron  
495 (ZVI) for enhanced treatment of chlorinated ethanes in permeable reactive barriers (PRBs). *Chem Eng J*

496 195–196:22–30. doi: 10.1016/j.cej.2012.04.026

497 Bhattacharjee S, Basnet M, Tufenkji N, Ghoshal S (2016) Effects of rhamnolipid and carboxymethylcellulose  
498 coatings on reactivity of palladium-doped nanoscale zerovalent iron particles. *Environ Sci Technol*  
499 50:1812–1820. doi: 10.1021/acs.est.5b05074

500 Bruton TA, Pycke BFG, Halden RU (2015) Effect of nanoscale zero-valent iron treatment on biological  
501 reductive dechlorination: A review of current understanding and research needs. *Crit Rev Environ Sci*  
502 *Technol* 45:1148–1175. doi: 10.1080/10643389.2014.924185

503 Butler EC, Hayes KF (1998) Effects of solution composition and pH on the reductive dechlorination of  
504 hexachloroethane by iron sulfide. *Environ Sci Technol* 32:1276–1284. doi: 10.1021/es9706864

505 Chaplin BP, Reinhard M, Schneider WF, Schüth C, Shapley JR, Strathmann TJ, Werth CJ (2012) Critical review  
506 of Pd-based catalytic treatment of priority contaminants in water. *Environ Sci Technol* 46:3655–3670. doi:  
507 10.1021/es204087q

508 Chronopoulou L, Palocci C, Valentino F, Pettiti I, Waclawek S, Černík M, Papini MP (2016) Stabilization of  
509 iron (micro)particles with polyhydroxybutyrate for in situ remediation applications. *Appl Sci* 6:417. doi:  
510 10.3390/app6120417

511 Comba S, Di Molfetta A, Sethi R (2011) A comparison between field applications of nano-, micro-, and  
512 millimetric zero-valent iron for the remediation of contaminated aquifers. *Water, Air, Soil Pollut* 215:595–  
513 607. doi: 10.1007/s11270-010-0502-1

514 Crane RA, Scott TB (2012) Nanoscale Zero-Valent Iron: Future Prospects for an Emerging Water Treatment  
515 Technology. *J Hazard Mater* 211:112–125. doi: 10.1016/j.jhazmat.2011.11.073

516 De Windt W, Aelterman P, Verstraete W (2005) Bioreductive deposition of palladium (0) nanoparticles on  
517 *Shewanella oneidensis* with catalytic activity towards reductive dechlorination of polychlorinated  
518 biphenyls. *Environ Microbiol* 7:314–325. doi: 10.1111/j.1462-2920.2005.00696.x

519 Dien NT, De Windt W, Buekens A, Chang MB (2013) Application of bimetallic iron (BioCAT slurry) for  
520 pentachlorophenol removal from sandy soil. *J Hazard Mater* 252:83–90. doi:  
521 10.1016/j.jhazmat.2013.02.029

- 522 Elliott DW, Zhang W (2001) Field assessment of nanoscale bimetallic particles for groundwater treatment.  
523 Environ Sci Technol 35:4922–4926. doi: 10.1021/es0108584
- 524 Fan D, O’Carroll DM, Elliott DW, Xiong Z, Tratnyek PG, Johnson RL, Garcia AN (2016) Selectivity of nano  
525 zerovalent iron in in situ chemical reduction: Challenges and improvements. Remediat J 26:27–40. doi:  
526 10.1002/rem.21481
- 527 Fang L, Xu C, Zhang W, Huang L-Z (2018) The important role of polyvinylpyrrolidone and Cu on enhancing  
528 dechlorination of 2,4-dichlorophenol by Cu/Fe nanoparticles: Performance and mechanism study. Appl  
529 Surf Sci 435:55–64. doi: 10.1016/j.apsusc.2017.11.084
- 530 Filip J, Karlický F, Marušák Z, Lazar P, Černík M, Otyepka M, Zbořil R (2014) Anaerobic reaction of nanoscale  
531 zerovalent iron with water: Mechanism and kinetics. J Phys Chem C 118:13817–13825. doi:  
532 10.1021/jp501846f
- 533 Fu F, Dionysiou DD, Liu H (2014) The use of zero-valent iron for groundwater remediation and wastewater  
534 treatment: A review. J Hazard Mater 267:194–205. doi: 10.1016/j.jhazmat.2013.12.062
- 535 Gillham RW, O’Hannesin SF (1994) Enhanced degradation of halogenated aliphatics by zero-valent iron.  
536 Ground Water 32:958–967. doi: 10.1111/j.1745-6584.1994.tb00935.x
- 537 Graham LJ, Jovanovic G (1999) Dechlorination of p-chlorophenol on a Pd/Fe catalyst in a magnetically  
538 stabilized fluidized bed; Implications for sludge and liquid remediation. Chem Eng Sci 54:3085–3093. doi:  
539 10.1016/S0009-2509(98)00393-5
- 540 Greenlee LF, Torrey JD, Amaro RL, Shaw JM (2012) Kinetics of zero valent iron nanoparticle oxidation in  
541 oxygenated water. Environ Sci Technol 46:12913–12920. doi: 10.1021/es303037k
- 542 Grieger KD, Fjordbøge A, Hartmann NB, Eriksson E, Bjerg PL, Baun A (2010) Environmental benefits and  
543 risks of zero-valent iron nanoparticles (nZVI) for in situ remediation: Risk mitigation or trade-off? J  
544 Contam Hydrol 118:165–183. doi: 10.1016/j.jconhyd.2010.07.011
- 545 Grittini C, Malcomson M, Fernando Q, Korte N (1995) Rapid dechlorination of polychlorinated biphenyls on the  
546 surface of a Pd/Fe bimetallic system. Environ Sci Technol 29:2898–2900. doi: 10.1021/es00011a029
- 547 Han J, Xin J, Zheng X, Kolditz O, Shao H (2016) Remediation of trichloroethylene-contaminated groundwater

548 by three modifier-coated microscale zero-valent iron. *Environ Sci Pollut Res* 23:14442–14450. doi:  
549 10.1007/s11356-016-6368-z

550 He F, Li Z, Shi S, Xu W, Sheng H, Gu Y, Jiang Y, Xi B (2018) Dechlorination of excess trichloroethene by  
551 bimetallic and sulfidated nanoscale zero-valent iron. *Environ Sci Technol* 52:8627–8637. doi:  
552 10.1021/acs.est.8B01735

553 He F, Zhao D (2008) Hydrodechlorination of trichloroethene using stabilized Fe-Pd nanoparticles: Reaction  
554 mechanism and effects of stabilizers, catalysts and reaction conditions. *Appl Catal B Environ* 84:533–540.  
555 doi: 10.1016/j.apcatb.2008.05.008

556 He F, Zhao D, Liu J, Roberts CB (2007) Stabilization of Fe–Pd nanoparticles with sodium carboxymethyl  
557 cellulose for enhanced transport and dechlorination of trichloroethylene in soil and groundwater. *Ind Eng*  
558 *Chem Res* 46:29–34. doi: 10.1021/ie0610896

559 He F, Zhao D, Paul C (2010) Field assessment of carboxymethyl cellulose stabilized iron nanoparticles for in  
560 situ destruction of chlorinated solvents in source zones. *Water Res* 44:2360–2370. doi:  
561 10.1016/j.watres.2009.12.041

562 Heck KN, Janesko BG, Scuseria GE, Halas NJ, Wong MS (2008) Observing metal-catalyzed chemical reactions  
563 in situ using surface-enhanced raman spectroscopy on Pd-Au nanoshells. *J Am Chem Soc* 130:16592–  
564 16600. doi: 10.1021/ja803556k

565 Herrero J, Puigserver D, Nijenhuis I, Kuntze K, Carmona JM (2019) Combined use of ISCR and biostimulation  
566 techniques in incomplete processes of reductive dehalogenation of chlorinated solvents. *Sci Total Environ*  
567 648:819–829. doi: 10.1016/j.scitotenv.2018.08.184

568 Howard PH (1989) *Handbook of Environmental Fate and Exposure Data for Organic Chemicals*. CRC Press

569 Huang B, Isse AA, Durante C, Wei C, Gennaro A (2012) Electrocatalytic properties of transition metals toward  
570 reductive dechlorination of polychloroethanes. *Electrochim Acta* 70:50–61. doi:  
571 10.1016/j.electacta.2012.03.009

572 Huang B, Qian W, Yu C, Wang T, Zeng G, Lei C (2016) Effective catalytic hydrodechlorination of o-, p- and m-  
573 chloronitrobenzene over Ni/Fe nanoparticles: Effects of experimental parameter and molecule structure on  
574 the reduction kinetics and mechanisms. *Chem Eng J* 306:607–618. doi: 10.1016/j.cej.2016.07.109



575 Hunting ER, Kampfraath AA (2013) Contribution of bacteria to redox potential (Eh) measurements in  
576 sediments. *Int J Environ Sci Technol* 10:55–62. doi: 10.1007/s13762-012-0080-4

577 Jiang G, Lan M, Zhang Z, Lv X, Lou Z, Xu X, Dong F, Zhang S (2017) Identification of active hydrogen species  
578 on palladium nanoparticles for an enhanced electrocatalytic hydrodechlorination of 2,4-dichlorophenol in  
579 water. *Environ Sci Technol* 51:7599–7605. doi: 10.1021/acs.est.7b01128

580 Jiang G, Wang K, Li J, Fu W, Zhang Z, Johnson G, Lv X, Zhang Y, Zhang S, Dong F (2018) Electrocatalytic  
581 hydrodechlorination of 2,4-dichlorophenol over palladium nanoparticles and its pH-mediated tug-of-war  
582 with hydrogen evolution. *Chem Eng J* 348:26–34. doi: 10.1016/j.cej.2018.04.173

583 Kaifas D, Malleret L, Kumar N, Fétimi W, Claeys-Bruno M, Sergent M, Doumenq P (2014) Assessment of  
584 potential positive effects of nZVI surface modification and concentration levels on TCE dechlorination in  
585 the presence of competing strong oxidants, using an experimental design. *Sci Total Environ* 481:335–342.  
586 doi: 10.1016/j.scitotenv.2014.02.04

587 Kim C, Ahn J-Y, Kim TY, Shin WS, Hwang I (2018) Activation of persulfate by nanosized zero-valent iron  
588 (NZVI): Mechanisms and transformation products of NZVI. *Environ Sci Technol* 52:3625–3633. doi:  
589 10.1021/acs.est.7b05847

590 Kim YH, Carraway ER (2003) Reductive dechlorination of TCE by zero valent bimetals. *Environ Technol*  
591 24:69–75. doi: 10.1080/09593330309385537

592 Kocur CM, Chowdhury AI, Sakulchaicharoen N, Boparai HK, Weber KP, Sharma P, Krol MM, Austrins L,  
593 Peace C, Sleep BE, O’Carroll DM (2014) Characterization of nZVI mobility in a field scale test. *Environ*  
594 *Sci Technol* 48:2862–2869. doi: 10.1021/es4044209

595 Kocur CMD, Lomheim L, Molenda O, Weber KP, Austrins LM, Sleep BE, Boparai HK, Edwards EA, O’Carroll  
596 DM (2016) Long-term field study of microbial community and dechlorinating activity following  
597 carboxymethyl cellulose-stabilized nanoscale zero-valent iron injection. *Environ Sci Technol* 50:7658–  
598 7670. doi: 10.1021/acs.est.6b01745

599 Koenig JC, Boparai HK, Lee MJ, O’Carroll DM, Barnes RJ, Manefield MJ (2016) Particles and enzymes:  
600 Combining nanoscale zero valent iron and organochlorine respiring bacteria for the detoxification of  
601 chloroethane mixtures. *J Hazard Mater* 308:106–112. doi: 10.1016/j.jhazmat.2015.12.036

602 Kumar N, Auffan M, Gattacceca J, Rose J, Olivi L, Borschneck D, Kvapil P, Jublot M, Kaifas D, Malleret L,  
603 Doumenq P, Bottero J-Y (2014) Molecular insights of oxidation process of iron nanoparticles:  
604 Spectroscopic, magnetic, and microscopic evidence. *Environ Sci Technol* 48:13888–13894. doi:  
605 10.1021/es503154q

606 Kumar N, Labille J, Bossa N, Auffan M, Doumenq P, Rose J, Bottero J-Y (2017) Enhanced transportability of  
607 zero valent iron nanoparticles in aquifer sediments: Surface modifications, reactivity, and particle traveling  
608 distances. *Environ Sci Pollut Res* 24:9269–9277. doi: 10.1007/s11356-017-8597-1

609 Lee C, Kim JY, Lee W II, Nelson KL, Yoon J, Sedlak DL (2008) Bactericidal effect of zero-valent iron  
610 nanoparticles on *Escherichia coli*. *Environ Sci Technol* 42:4927–4933. doi: 10.1021/es800408u

611 Lien H-L, Zhang W (2007) Nanoscale Pd/Fe bimetallic particles: Catalytic effects of palladium on  
612 hydrodechlorination. *Appl Catal B Environ* 77:110–116. doi: 10.1016/j.apcatb.2007.07.014

613 Lien H-L, Zhang W (1999) Transformation of chlorinated methanes by nanoscale iron particles. *J Environ Eng*  
614 125:1042–1047. doi: 10.1061/(ASCE)0733-9372(1999)125:11(1042)

615 Lien H-L, Zhang W (2005) Hydrodechlorination of chlorinated ethanes by nanoscale Pd/Fe bimetallic particles.  
616 *J Environ Eng* 131:4–10. doi: 10.1061/(ASCE)0733-9372(2005)131:1(4)

617 Lin CJ, Lo S-L (2005) Effects of iron surface pretreatment on sorption and reduction kinetics of  
618 trichloroethylene in a closed batch system. *Water Res* 39:1037–1046. doi: 10.1016/j.watres.2004.06.035

619 Ling L, Huang X, Li M, Zhang W (2017) Mapping the reactions in a single zero-valent iron nanoparticle.  
620 *Environ Sci Technol* 51:14293–14300. doi: 10.1021/acs.est.7b02233

621 Ling L, Zhang W (2014) Structures of Pd–Fe(0) Bimetallic nanoparticles near 0.1 nm resolution. *RSC Adv*  
622 4:33861. doi: 10.1039/C4RA04311A

623 Liu A, Liu J, Han J, Zhang W (2017) Evolution of nanoscale zero-valent iron (nZVI) in water: Microscopic and  
624 spectroscopic evidence on the formation of nano- and micro-structured iron oxides. *J Hazard Mater*  
625 322:129–135. doi: 10.1016/j.jhazmat.2015.12.070

626 Liu A, Liu J, Pan B, Zhang W (2014a) Formation of lepidocrocite ( $\gamma$ -FeOOH) from oxidation of nanoscale zero-  
627 valent iron (nZVI) in oxygenated water. *RSC Adv* 4:57377–57382. doi: 10.1039/C4RA08988J

628 Liu A, Zhang W (2014) Fine structural features of nanoscale zero-valent iron characterized by spherical  
629 aberration corrected scanning transmission electron microscopy (Cs-STEM). *Analyst* 139:4512–4518. doi:  
630 10.1039/C4AN00679H

631 Liu R, Zhao H, Zhao X, He Z, Lai Y, Shan W, Bekana D, Li G, Liu J (2018) Defect sites in ultrathin Pd  
632 nanowires facilitate the highly efficient electrochemical hydrodechlorination of pollutants by H<sup>\*</sup>ads.  
633 *Environ Sci Technol* 52:9992–10002. doi: 10.1021/acs.est.8b02740

634 Liu W-J, Qian T-T, Jiang H (2014b) Bimetallic Fe nanoparticles: Recent advances in synthesis and application  
635 in catalytic elimination of environmental pollutants. *Chem Eng J* 236:448–463. doi:  
636 10.1016/j.cej.2013.10.062

637 Liu Y, Lowry G V. (2006) Effect of particle age (Fe<sup>0</sup> content) and solution pH on NZVI reactivity: H<sub>2</sub> evolution  
638 and TCE dechlorination. *Environ Sci Technol* 40:6085–6090. doi: 10.1021/es060685o

639 Louie SM, Tilton RD, Lowry G V (2016) Critical review: Impacts of macromolecular coatings on critical  
640 physicochemical processes controlling environmental fate of nanomaterials. *Environ Sci Nano* 3:283–310.  
641 doi: 10.1039/C5EN00104H

642 Lowry G V, Reinhard M (1999) Hydrodehalogenation of 1- to 3-carbon halogenated organic compounds in  
643 water using a palladium catalyst and hydrogen gas. *Environ Sci Technol* 33:1905–1910. doi:  
644 10.1021/es980963m

645 Martin JE, Herzing AA, Yan W, Li X, Koel BE, Kiely CJ, Zhang W (2008) Determination of the oxide layer  
646 thickness in core–shell zerovalent iron nanoparticles. *Langmuir* 24:4329–4334. doi: 10.1021/la703689K

647 Mu Y, Jia F, Ai Z, Zhang L (2017) Iron oxide shell mediated environmental remediation properties of nano zero-  
648 valent iron. *Environ Sci Nano* 4:27–45. doi: 10.1039/C6EN00398B

649 Muftikian R, Nebesny K, Fernando Q, Korte N (1996) X-ray photoelectron spectra of the palladium–iron  
650 bimetallic surface used for the rapid dechlorination of chlorinated organic environmental contaminants.  
651 *Environ Sci Technol* 30:3593–3596. doi: 10.1021/es960289D

652 Noubactep C (2008) A critical review on the process of contaminant removal in Fe<sup>0</sup>-H<sub>2</sub>O systems. *Environ*  
653 *Technol* 29:909–920. doi: 10.1080/09593330802131602

654 Noubactep C, Caré S, Crane R (2012) Nanoscale metallic iron for environmental remediation: Prospects and  
655 limitations. *Water Air Soil Pollut* 223:1363–1382. doi: 10.1007/s11270-011-0951-1

656 Nurmi JT, Tratnyek PG, Sarathy V, Baer DR, Amonette JE, Pecher K, Wang C, Linehan JC, Matson DW, Penn  
657 RL, Driessen MD (2005) Characterization and properties of metallic iron nanoparticles: Spectroscopy,  
658 electrochemistry, and kinetics. *Environ Sci Technol* 39:1221–1230. doi: 10.1021/es049190U

659 O’Hannesin SF, Gillham RW (1998) Long-term performance of an in situ “iron wall” for remediation of VOCs.  
660 *Ground Water* 36:164–170. doi: 10.1111/j.1745-6584.1998.tb01077.x

661 O ’Carroll D, Sleep B, Krol M, Boparai H, Kocur C (2013) Nanoscale zero valent iron and bimetallic particles  
662 for contaminated site remediation. *Adv Water Resour* 51:104–122. doi: 10.1016/j.advwatres.2012.02.005

663 Papaderakis A, Tsiplakides D, Balomenou S, Sotiropoulos S (2017) Probing the hydrogen adsorption affinity of  
664 Pt and Ir by surface interrogation scanning electrochemical microscopy (SI-SECM). *Electrochem Commun*  
665 83:77–80. doi: 10.1016/j.elecom.2017.09.003

666 Patterson E V., Cramer CJ, Truhlar DG (2001) Reductive dechlorination of hexachloroethane in the  
667 environment: Mechanistic studies via computational electrochemistry. *J Am Chem Soc* 123:2025–2031.  
668 doi: 10.1021/ja0035349

669 Phenrat T, Liu Y, Tilton RD, Lowry G V (2009) Adsorbed polyelectrolyte coatings decrease Fe(0) nanoparticle  
670 reactivity with TCE in water: Conceptual model and mechanisms. *Environ Sci Technol* 43:1507–14. doi:  
671 10.1021/es802187d

672 Phenrat T, Saleh N, Sirk K, Kim H-J, Tilton RD, Lowry G V. (2008) Stabilization of aqueous nanoscale  
673 zerovalent iron dispersions by anionic polyelectrolytes: Adsorbed anionic polyelectrolyte layer properties  
674 and their effect on aggregation and sedimentation. *J Nanoparticle Res* 10:795–814. doi: 10.1007/s11051-  
675 007-9315-6

676 Pierro L, Matturro B, Rossetti S, Sagliaschi M, Sucato S, Alesi E, Bartsch E, Arjmand F, Papini MP (2017)  
677 Polyhydroxyalkanoate as a slow-release carbon source for in situ bioremediation of contaminated aquifers:  
678 from laboratory investigation to pilot-scale testing in the field. *N Biotechnol* 37:60–68. doi:  
679 10.1016/j.nbt.2016.11.004

680 Pilling MJ, Seakins PW (1995) *Reaction Kinetics*. Oxford University Press, New York, NY, USA.

681 Pizarro S, Araya M, Delgadillo A (2018) Hexachloroethane reduction catalyzed by cobaloximes. Effect of the  
682 substituents on the equatorial ligands. *Polyhedron* 141:94–99. doi: 10.1016/j.poly.2017.11.005

683 Reddy AVB, Yusop Z, Jaafar J, Reddy YVM, Aris A Bin, Majid ZA, Talib J, Madhavi G (2016) Recent  
684 progress on Fe-based nanoparticles: Synthesis, properties, characterization and environmental applications.  
685 *J Environ Chem Eng* 4:3537–3553. doi: 10.1016/j.jece.2016.07.035

686 Reddy KR, Khodadoust AP, Darko-Kagya K (2014) Transport and reactivity of lactate-modified nanoscale iron  
687 particles for remediation of DNT in subsurface soils. *J Environ Eng* 140:04014042. doi:  
688 10.1061/(ASCE)EE.1943-7870.0000870

689 Rodrigues R, Betelu S, Colombano S, Masselot G, Tzedakis T, Ignatiadis I (2017a) Reductive dechlorination of  
690 hexachlorobutadiene by a Pd/Fe microparticle suspension in dissolved lactic acid polymers: Degradation  
691 mechanism and kinetics. *Ind Eng Chem Res* 56:12092–12100. doi: 10.1021/acs.iecr.7b03012

692 Rodrigues R, Betelu S, Colombano S, Masselot G, Tzedakis T, Ignatiadis I (2017b) Influence of temperature and  
693 surfactants on the solubilization of hexachlorobutadiene and hexachloroethane. *J Chem Eng Data* 62:3252–  
694 3260. doi: 10.1021/acs.jced.7b00320

695 Sabot R, Jeannin M, Gadouleau M, Guo Q, Sicre E, Refait P (2007) Influence of lactate ions on the formation of  
696 rust. *Corros Sci* 49:1610–1624. doi: 10.1016/j.corsci.2006.10.004

697 Sarathy V, Tratnyek PG, Nurmi JT, Baer DR, Amonette JE, Chun CL, Penn RL, Reardon EJ (2008) Aging of  
698 iron nanoparticles in aqueous solution: Effects on structure and reactivity. *J Phys Chem C* 112:2286–2293.  
699 doi: 10.1021/jp0777418

700 Schöftner P, Waldner G, Lottermoser W, Stöger-Pollach M, Freitag P, Reichenauer TG (2015) Electron  
701 efficiency of nZVI does not change with variation of environmental parameters. *Sci Total Environ* 535:69–  
702 78. doi: 10.1016/j.scitotenv.2015.05.033

703 Shi Z, Fan D, Johnson RL, Tratnyek PG, Nurmi JT, Wu Y, Williams KH (2015) Methods for characterizing the  
704 fate and effects of nano zerovalent iron during groundwater remediation. *J Contam Hydrol* 181:17–35. doi:  
705 10.1016/j.jconhyd.2015.03.004

706 Shi Z, Nurmi JT, Tratnyek PG (2011) Effects of nano Zero-valent iron on oxidation–reduction potential. *Environ*  
707 *Sci Technol* 45:1586–1592. doi: 10.1021/es103185t

708 Shih Y, Chen M-Y, Su Y-F (2011) Pentachlorophenol reduction by Pd/Fe bimetallic nanoparticles: Effects of  
709 copper, nickel, and ferric cations. *Appl Catal B Environ* 105:24–29. doi: 10.1016/j.apcatb.2011.03.024

710 Song H, Carraway ER (2005) Reduction of chlorinated ethanes by nanosized zero-valent iron: Kinetics,  
711 pathways, and effects of reaction conditions. *Environ Sci Technol* 39:6237–6245. doi: 10.1021/es048262e

712 Sriwatanapongse W, Reinhard M, Klug CA (2006) Reductive hydrodechlorination of trichloroethylene by  
713 palladium-on-alumina catalyst: <sup>13</sup>C solid-state NMR study of surface reaction precursors. *Langmuir*  
714 22:4158–4164. doi: 10.1021/la053087g

715 Stefaniuk M, Oleszczuk P, Ok YS (2016) Review on nano zerovalent iron (nZVI): From synthesis to  
716 environmental applications. *Chem Eng J* 287:618–632. doi: 10.1016/j.cej.2015.11.046

717 Stringer R, Johnston P (2001) *Chlorine and the Environment: An Overview of the Chlorine Industry*. Kluwer  
718 Academic Publishers

719 Sun Y-P, Li X, Cao J, Zhang W, Wang HP (2006) Characterization of zero-valent iron nanoparticles. *Adv*  
720 *Colloid Interface Sci* 120:47–56. doi: 10.1016/j.cis.2006.03.001

721 Sun Y, Li J, Huang T, Guan X (2016) The influences of iron characteristics, operating conditions and solution  
722 chemistry on contaminants removal by zero-valent iron: A review. *Water Res* 100:277–295. doi:  
723 10.1016/j.watres.2016.05.031

724 Tang F, Xin J, Zheng X, Zheng T, Yuan X, Kolditz O (2017a) Effect of solution pH on aging dynamics and  
725 Surface structural evolution of mZVI particles: H<sub>2</sub> production and spectroscopic/microscopic evidence.  
726 *Environ Sci Pollut Res* 1–11. doi: 10.1007/s11356-017-9976-3

727 Tang S, Wang X, Liu S, Yang H, Xie YF, Yang X (2017b) Mechanism and kinetics of halogenated compound  
728 removal by metallic iron: Transport in solution, diffusion and reduction within corrosion films.  
729 *Chemosphere* 178:119–128. doi: 10.1016/j.chemosphere.2017.03.006

730 Tosco T, Papini MP, Cruz Viggi C, Sethi R (2014) Nanoscale zerovalent iron particles for groundwater  
731 remediation: A review. *J Clean Prod* 77:10–21. doi: 10.1016/j.jclepro.2013.12.026

732 Velimirovic M, Auffan M, Carniato L, Batka VM, Schmid D, Wagner S, Borschneck D, Proux O, von der  
733 Kammer F, Hofmann T (2018) Effect of field site hydrogeochemical conditions on the corrosion of milled

734 zerovalent iron particles and their dechlorination efficiency. *Sci Total Environ* 618:1619–1627. doi:  
735 10.1016/j.scitotenv.2017.10.002

736 Velimirovic M, Carniato L, Simons Q, Schoups G, Seuntjens P, Bastiaens L (2014) Corrosion rate estimations of  
737 microscale zerovalent iron particles via direct hydrogen production measurements. *J Hazard Mater* 270:18–  
738 26. doi: 10.1016/j.jhazmat.2014.01.034

739 Velimirovic M, Chen H, Simons Q, Bastiaens L (2012) Reactivity recovery of guar gum coupled mZVI by  
740 means of enzymatic breakdown and rinsing. *J Contam Hydrol* 142–143:1–10. doi:  
741 10.1016/j.jconhyd.2012.09.003

742 Velimirovic M, Larsson P-O, Simons Q, Bastiaens L (2013a) Reactivity screening of microscale zerovalent irons  
743 and iron sulfides towards different CAHs under standardized experimental conditions. *J Hazard Mater*  
744 252–253:204–212. doi: 10.1016/j.jhazmat.2013.02.047

745 Velimirovic M, Larsson P-O, Simons Q, Bastiaens L (2013b) Impact of carbon, oxygen and sulfur content of  
746 microscale zerovalent iron particles on its reactivity towards chlorinated aliphatic hydrocarbons.  
747 *Chemosphere* 93:2040–2045. doi: 10.1016/j.chemosphere.2013.07.034

748 Velimirovic M, Simons Q, Bastiaens L (2015) Use of CAH-degrading bacteria as test-organisms for evaluating  
749 the impact of fine zerovalent iron particles on the anaerobic subsurface environment. *Chemosphere*  
750 134:338–345. doi: 10.1016/j.chemosphere.2015.04.068

751 Voogt EH, Mens AJM, Gijzeman OLJ, Geus JW (1996) XPS analysis of palladium oxide layers and particles.  
752 *Surf Sci* 350:21–31. doi: 10.1016/0039-6028(96)01028-X

753 Wang J, Chu L (2016) Biological nitrate removal from water and wastewater by solid-phase denitrification  
754 process. *Biotechnol Adv* 34:1103–1112. doi: 10.1016/j.biotechadv.2016.07.001

755 Wang X, Chen C, Chang Y, Liu H (2009) Dechlorination of chlorinated methanes by Pd/Fe bimetallic  
756 nanoparticles. *J Hazard Mater* 161:815–823. doi: 10.1016/j.jhazmat.2008.04.027

757 Wei Y-T, Wu S-C, Chou C-M, Che C-H, Tsai S-M, Lien H-L (2010) Influence of nanoscale zero-valent iron on  
758 geochemical properties of groundwater and vinyl chloride degradation: A field case study. *Water Res*  
759 44:131–140. doi: 10.1016/j.watres.2009.09.012

760 Wei Y-T, Wu S, Yang S-W, Che C-H, Lien H-L, Huang D-H (2012) Biodegradable surfactant stabilized  
761 nanoscale zero-valent iron for in situ treatment of vinyl chloride and 1,2-dichloroethane. *J Hazard Mater*  
762 211–212:373–380. doi: 10.1016/j.jhazmat.2011.11.018

763 Wu DL, Liu YX, Liu ZG, Ma LM (2014) Dechlorination of hexachloroethane in water using iron shavings and  
764 amended iron shavings: Kinetics and pathways. *J Chem* 2014:1–9. doi: 10.1155/2014/325879

765 Xie Y, Cwiertny DM (2013) Chlorinated solvent transformation by palladized zerovalent iron: Mechanistic  
766 insights from reductant loading studies and solvent kinetic isotope effects. *Environ Sci Technol* 47:7940–  
767 7948. doi: 10.1021/es401481a

768 Xu Y, Wang C, Hou J, Wang P, You G, Miao L, Lv B, Yang Y, Zhang F (2017) Application of zero valent iron  
769 coupling with biological process for wastewater treatment: A review. *Rev Environ Sci Bio/Technology* 1–  
770 27. doi: 10.1007/s11157-017-9445-y

771 Yan W, Herzing AA, Li X, Kiely CJ, Zhang W (2010) Structural evolution of Pd-doped nanoscale zero-valent  
772 iron (nZVI) in aqueous media and implications for particle aging and reactivity. *Environ Sci Technol*  
773 44:4288–4294. doi: 10.1021/es100051q

774 Yan W, Lien H-L, Koel BE, Zhang W (2013) Iron nanoparticles for environmental clean-up: Recent  
775 developments and future outlook. *Environ Sci Process Impacts* 15:63–77. doi: 10.1039/C2EM30691C

776 Yang Y, Cápiro NL, Marcet TF, Yan J, Pennell KD, Löffler FE (2017a) Organohalide respiration with  
777 chlorinated ethenes under low pH conditions. *Environ Sci Technol* 51:8579–8588. doi:  
778 10.1021/acs.est.7b01510

779 Yang Y, Cápiro NL, Yan J, Marcet TF, Pennell KD, Löffler FE (2017b) Resilience and recovery of  
780 dehalococcoides mccartyi following low pH exposure. *FEMS Microbiol Ecol* 93:fix130. doi:  
781 10.1093/femsec/fix130

782 Yu R-F, Chi F-H, Cheng W-P, Chang J-C (2014) Application of pH, ORP, and DO monitoring to evaluate  
783 chromium(VI) removal from wastewater by the nanoscale zero-valent iron (nZVI) process. *Chem Eng J*  
784 255:568–576. doi: 10.1016/j.cej.2014.06.002

785 Zhang W (2003) Nanoscale iron particles for environmental remediation: An overview. *J Nanoparticle Res*  
786 5:323–332. doi: 10.1023/A:1025520116015



- 787 Zhao X, Liu W, Cai Z, Han B, Qian T, Zhao D (2016) An overview of preparation and applications of stabilized  
788 zero-valent iron nanoparticles for soil and groundwater remediation. *Water Res* 100:245–266. doi:  
789 10.1016/j.watres.2016.05.019
- 790 Zhu B-W, Lim T-T, Feng J (2008) Influences of amphiphiles on dechlorination of a trichlorobenzene by  
791 nanoscale Pd/Fe: Adsorption, reaction kinetics, and interfacial interactions. *Environ Sci Technol* 42:4513–  
792 4519. doi: 10.1021/es800227r
- 793 Zhu C, Zhu F, Liu C, Chen N, Zhou D, Fang G, Gao J (2018) Reductive hexachloroethane degradation by  
794 S<sub>2</sub>O<sub>8</sub><sup>2-</sup> with thermal activation of persulfate under anaerobic conditions. *Environ Sci Technol* 52:8548–  
795 8557. doi: 10.1021/acs.est.7b06279
- 796

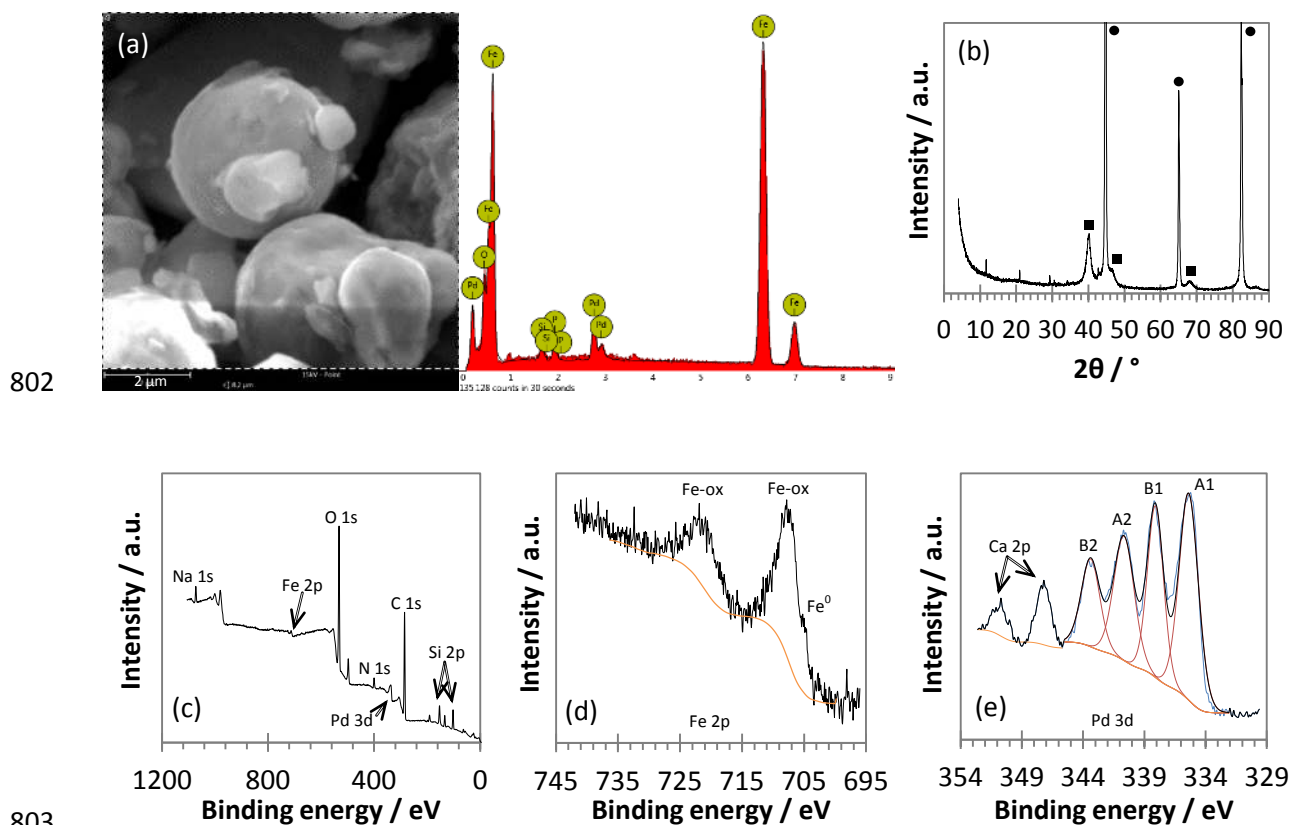
797 **List of tables**798 **Table 1** Pseudo-first order rate constants for HCA degradation under the different experimental conditions

799 (effects of Pd-mZVI dosage, temperature, HCA initial concentration and PLA content)

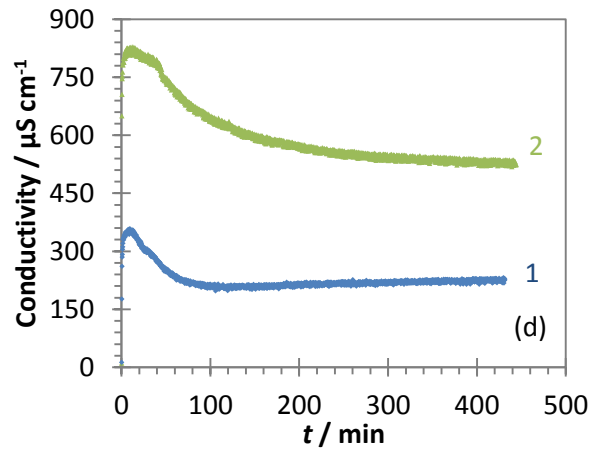
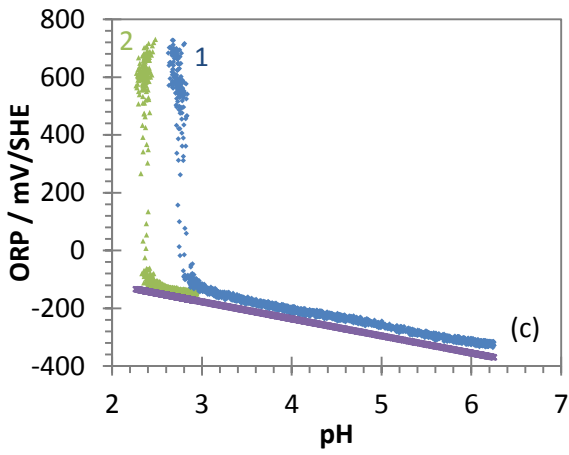
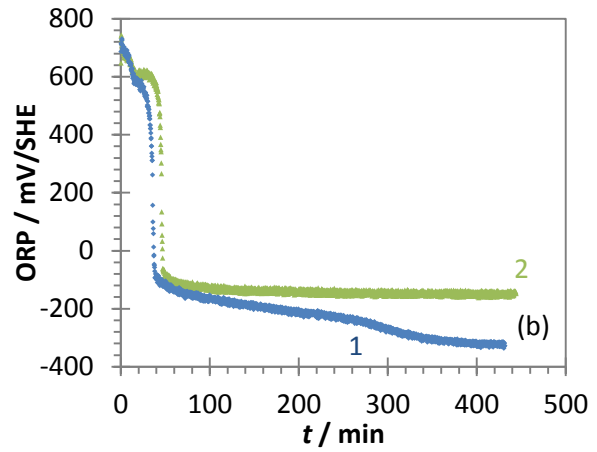
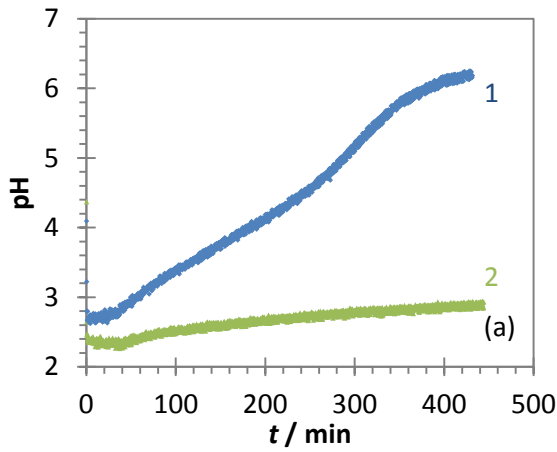
Figure number	$m_{\text{Pd-mZVI}}$ (mg)	$T$ (°C)	$[\text{HCA}]_0$ (mg L <sup>-1</sup> )	$m_{\text{PLA}}$ (mg)	$k_{\text{obs}}$ (Eq. 12) (min <sup>-1</sup> )
4	150	25	10	850	0.002 ( $R^2 = 0.474$ )
	375	25	10	850	0.004 ( $R^2 = 0.860$ )
4, 5, 6, 7	600	25	10	850	0.035 ( $R^2 = 0.975$ )
5	600	12	10	850	0.004 ( $R^2 = 0.970$ )
	600	35	10	850	0.093 ( $R^2 = 0.939$ )
6	600	25	5	850	0.036 ( $R^2 = 0.940$ )
	600	25	20	850	0.010 ( $R^2 = 0.972$ )
7	600	25	10	1 700	0.030 ( $R^2 = 0.938$ )
	600	25	10	3 400	0.025 ( $R^2 = 0.951$ )

800

801 **List of figures**



804 **Fig. 1** Characterization of Pd-mZVI particles before reaction. (a) SEM image with EDS spectrum. The atomic  
 805 concentration in the entire area is: Fe = 77.4%, O = 16.3%, Pd = 3.3%, P = 1.8%, Si = 1.2%; (b) X-ray  
 806 diffraction pattern, where solid circles and squares represent Fe<sup>0</sup> and Pd<sup>0</sup>, respectively; X-ray photoelectron  
 807 spectra: (c) Survey scan, (d) Fe 2p, (e) Pd 3d



808

809

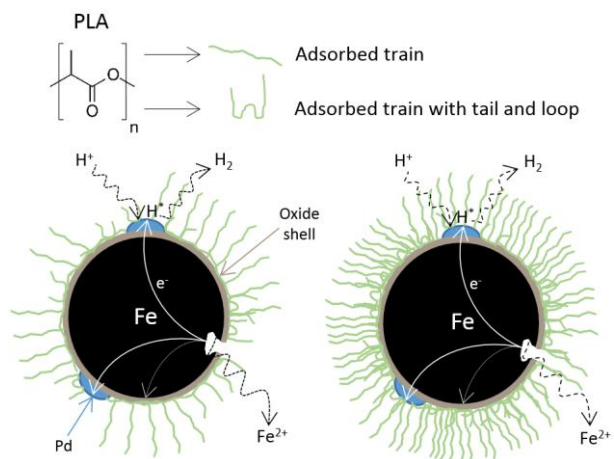
810

◆ (1) = 850 mg PLA, ▲ (2) = 3400 mg PLA, × = H<sup>+</sup>/H<sub>2</sub> redox couple

811 **Fig. 2** Monitoring of the aqueous corrosion in the Pd-mZVI/PLA/H<sub>2</sub>O system without opening of the reactor.

812 (a) Evolution of pH with time, (b) Evolution of ORP with time, (c) Evolution of ORP with pH, (d) Evolution of

813 conductivity with time. Experimental conditions:  $m_{\text{Pd-mZVI}} = 600 \text{ mg}$ ,  $T = 25 \text{ }^\circ\text{C}$

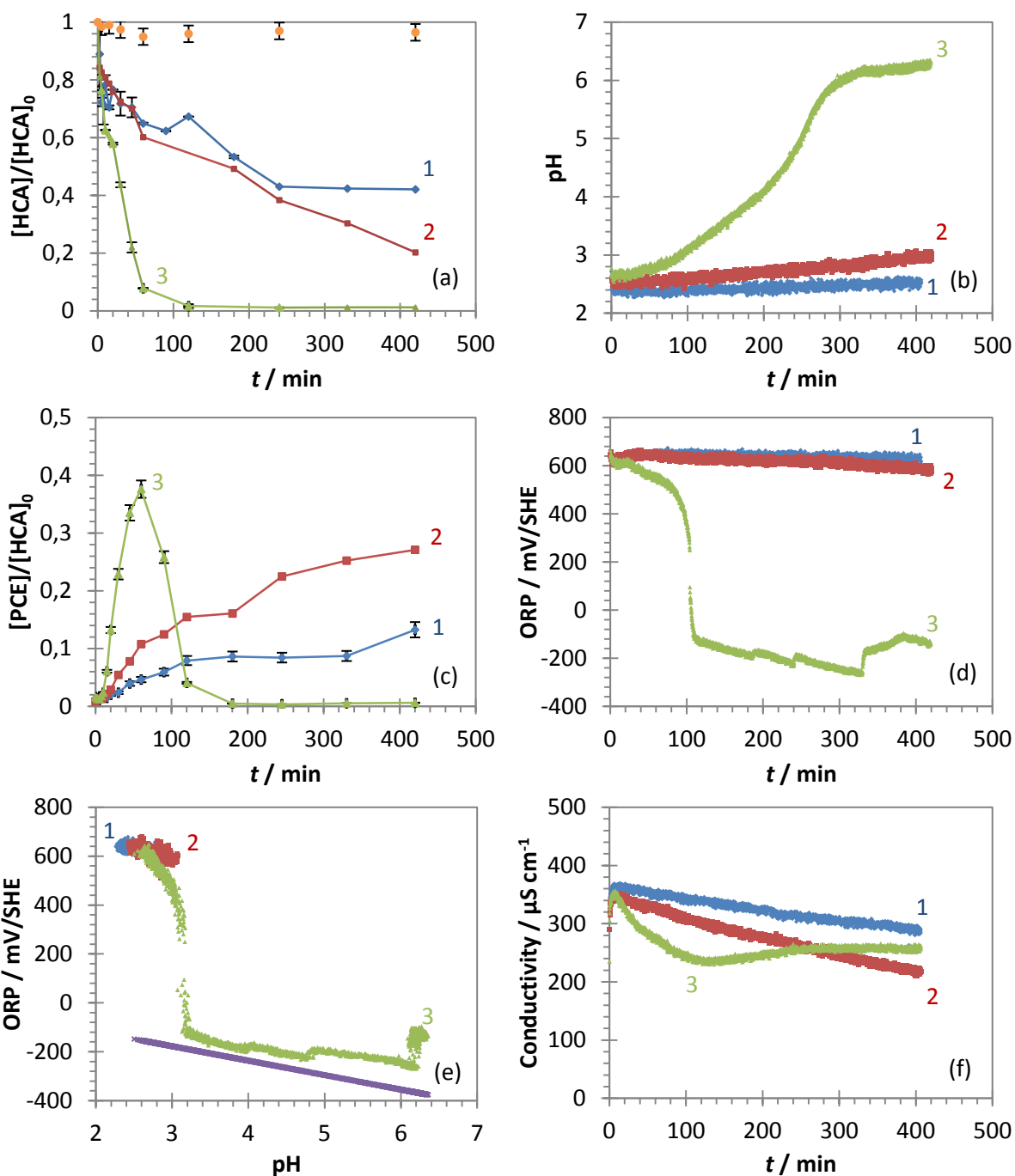


814

815 **Fig. 3** Schematic illustration of the Pd-mZVI/PLA/H<sub>2</sub>O system, with 850 mg (left) and 3400 mg (right) of PLA.

816 Depending on the adsorbed PLA on the surface, it is represented mainly as adsorbed train or as an extended layer

817 of adsorbed train with tails and loops.



818

819

820

821

◆ (1) = 150 mg Pd-mZVI, ■ (2) = 375 mg Pd-mZVI, ▲ (3) = 600 mg Pd-mZVI, ○ = blank, × =  $H^+/H_2$  redox couple

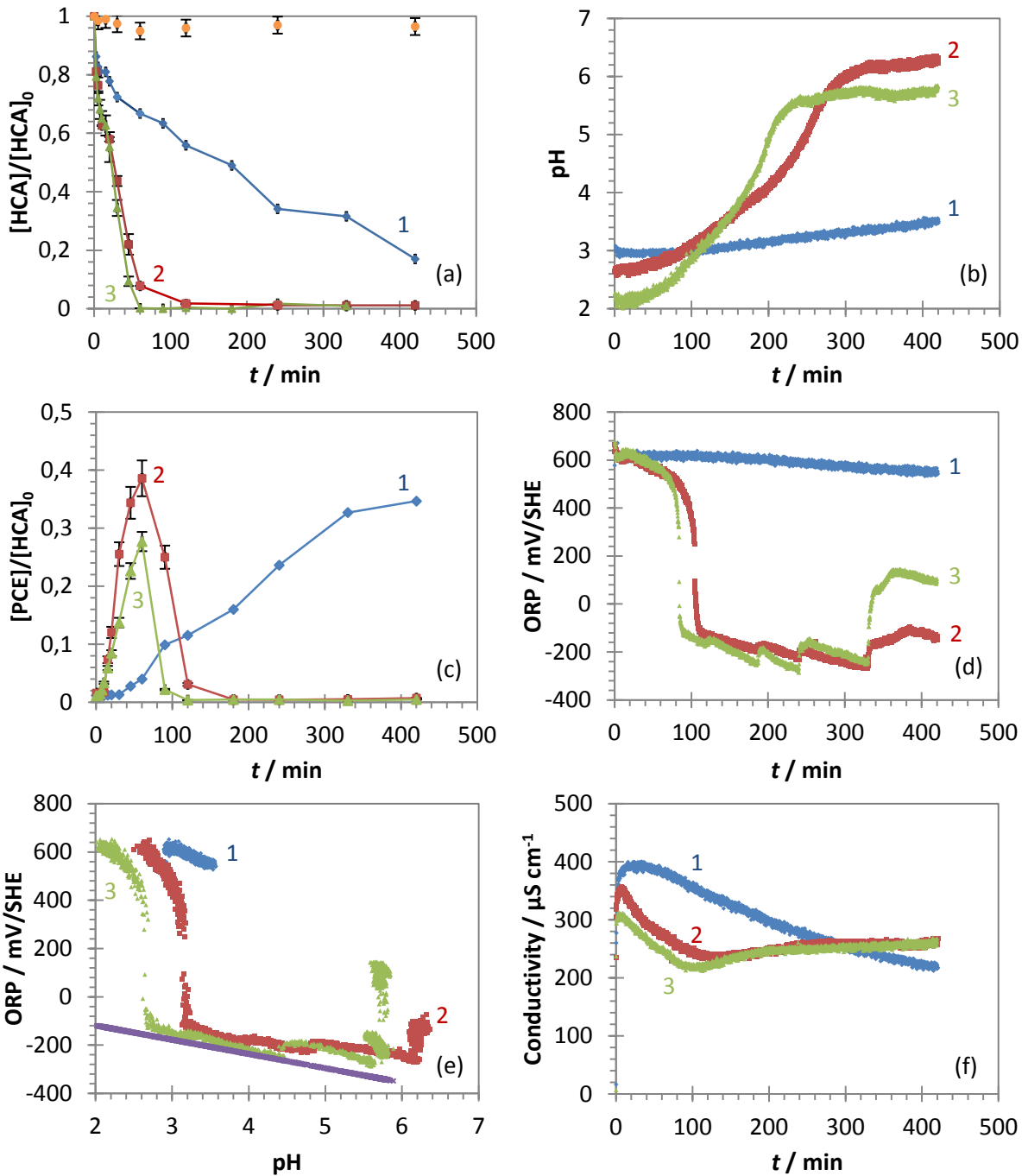
822 **Fig. 4** Effects of Pd-mZVI dosage on HCA dechlorination in the Pd-mZVI/PLA/HCA/ $H_2O$  system. (a) Evolution

823 of HCA concentration with time, (b) Evolution of pH with time, (c) Evolution of PCE concentration with time,

824 (d) Evolution of ORP with time, (e) Evolution of ORP with pH, (f) Evolution of conductivity with time.

825 Experimental conditions:  $[HCA]_0 = 10 \text{ mg L}^{-1}$ ,  $m_{PLA} = 850 \text{ mg}$ ,  $T = 25 \text{ }^\circ\text{C}$ . Error bars in parts a and c represent

826 standard deviation for  $n = 2$



827

828

829

830

◆ (1) = 12 °C, ■ (2) = 25 °C, ▲ (3) = 35 °C, ● = blank, × = H<sup>+</sup>/H<sub>2</sub> redox couple

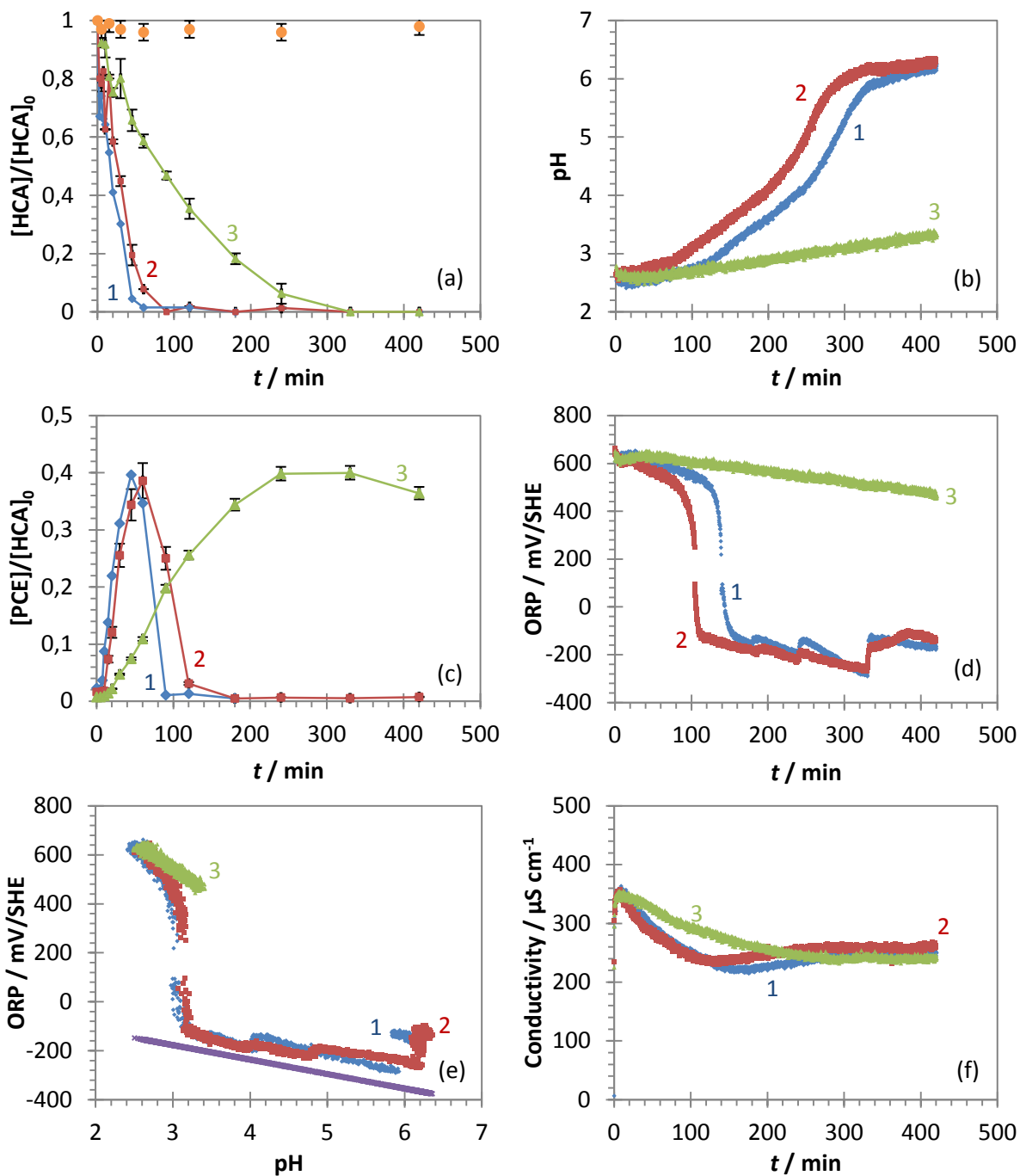
831 **Fig. 5** Effects of temperature on HCA dechlorination in the Pd-mZVI/PLA/HCA/H<sub>2</sub>O system. (a) Evolution of

832 HCA concentration with time, (b) Evolution of pH with time, (c) Evolution of PCE concentration with time, (d)

833 Evolution of ORP with time, (e) Evolution of ORP with pH, (f) Evolution of conductivity with time.

834 Experimental conditions: [HCA]<sub>0</sub> = 10 mg L<sup>-1</sup>, m<sub>Pd-mZVI</sub> = 600 mg, m<sub>PLA</sub> = 850 mg. Error bars in parts a and c

835 represent standard deviation for n = 2



836

837

838

839

◆ (1) = 5 mg L<sup>-1</sup>, ■ (2) = 10 mg L<sup>-1</sup>, ▲ (3) = 20 mg L<sup>-1</sup>, ● = blank, × = H<sup>+</sup>/H<sub>2</sub> redox couple

840 **Fig. 6** Effects of initial HCA concentration on its dechlorination in the Pd-mZVI/PLA/HCA/H<sub>2</sub>O system. (a)

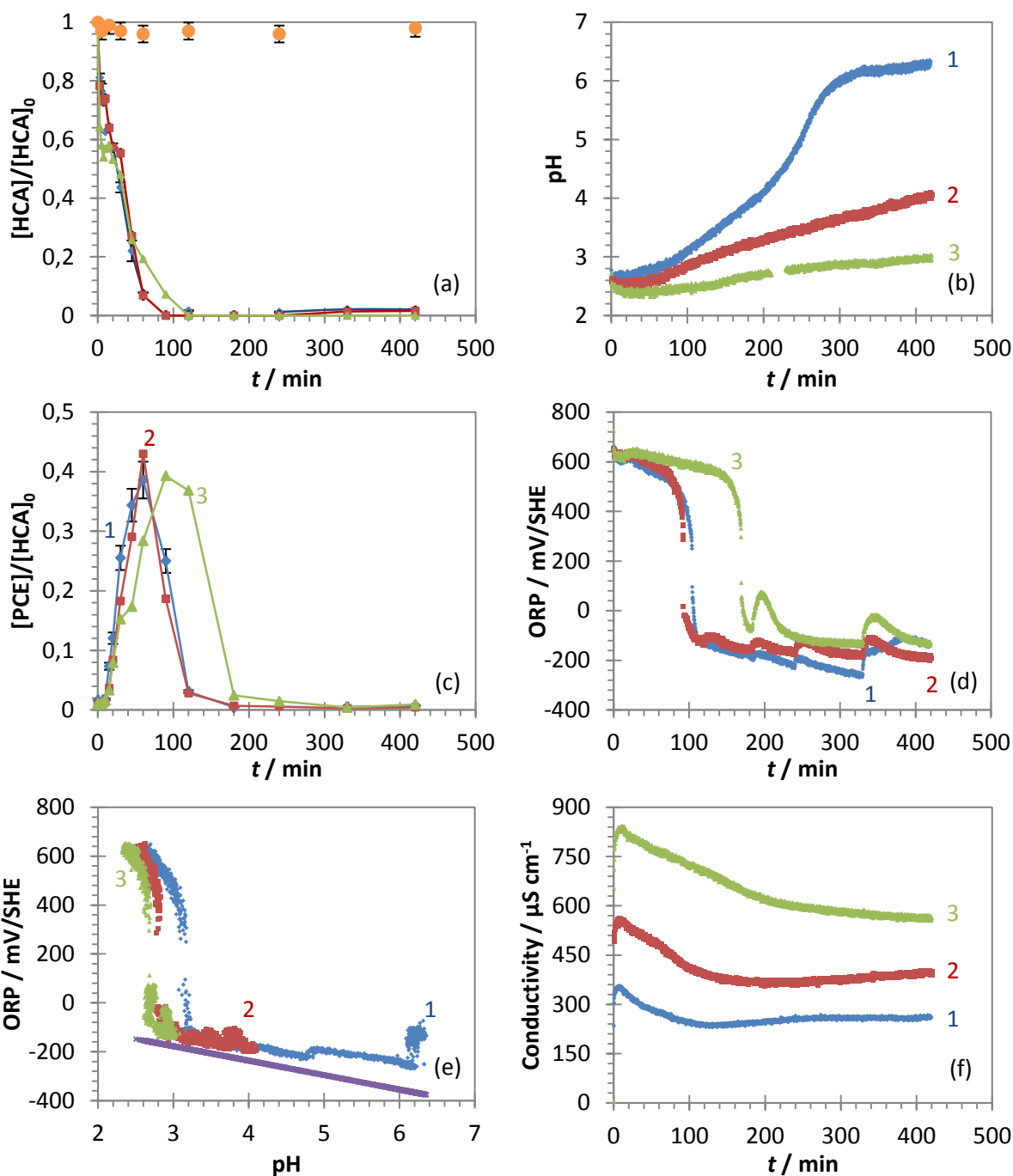
841 Evolution of HCA concentration with time, (b) Evolution of pH with time, (c) Evolution of PCE concentration

842 with time, (d) Evolution of ORP with time, (e) Evolution of ORP with pH, (f) Evolution of conductivity with

843 time. Experimental conditions:  $m_{\text{Pd-mZVI}} = 600$  mg,  $m_{\text{PLA}} = 850$  mg,  $T = 25$  °C. Error bars in parts a and c

844 represent standard deviation for  $n = 2$





845

846

847

848

◆ (1) = 850 mg PLA, ■ (2) = 1700 mg PLA, ▲ (3) = 3400 mg PLA, ● = blank, × =  $H^+/H_2$  redox couple

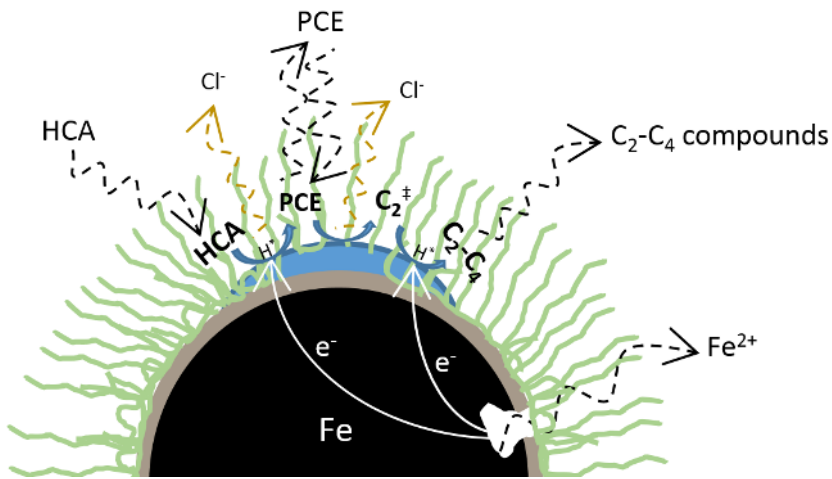
849 **Fig. 7** Influence of PLA content on HCA dechlorination in the Pd-mZVI/PLA/HCA/ $H_2O$  system. (a) Evolution

850 of HCA concentration with time, (b) Evolution of pH with time, (c) Evolution of PCE concentration with time,

851 (d) Evolution of ORP with time, (e) Evolution of ORP with pH, (f) Evolution of conductivity with time.

852 Experimental conditions:  $[HCA]_0 = 10 \text{ mg L}^{-1}$ ,  $m_{Pd-mZVI} = 600 \text{ mg}$ ,  $T = 25 \text{ }^\circ\text{C}$ . Error bars in parts a and c represent

853 standard deviation for  $n = 2$



854

855 **Fig. 8** Schematic illustration of reductive HCA dechlorination in the Pd-mZVI/PLA/HCA/H<sub>2</sub>O system.

856 Reactions proposed in Fig. 3 (production of atomic hydrogen H<sup>•</sup>) and in this figure (HCA dechlorination) may

857 occur simultaneously